Energy and AI 16 (2024) 100370

Contents lists available at ScienceDirect

Energy and AI

journal homepage: www.elsevier.com/locate/egyai

Machine and deep learning driven models for the design of heat exchangers with micro-finned tubes

Emad Efatinasab [a,1], Nima Irannezhad [b,1], Mirco Rampazzo [a], Andrea Diani [b,*]

[a] Department of Information Engineering, University of Padova, Via Gradenigo 6/b, Padova, 35131, PD, Italy
[b] Department of Industrial Engineering, University of Padova, Via Venezia 1, Padova, 35131, PD, Italy

HIGHLIGHTS

- Review on the application of AI for heat transfer and pressure drop prediction.
- Assembling 1192 flow condensation data points inside micro finned tubes.
- Categorization of inputs as dimensional and dimensionless parameters.
- Accuracy analyses of various ML and DL models.
- Assessment of interpretability of ANN model using SHAP library.

GRAPHICAL ABSTRACT

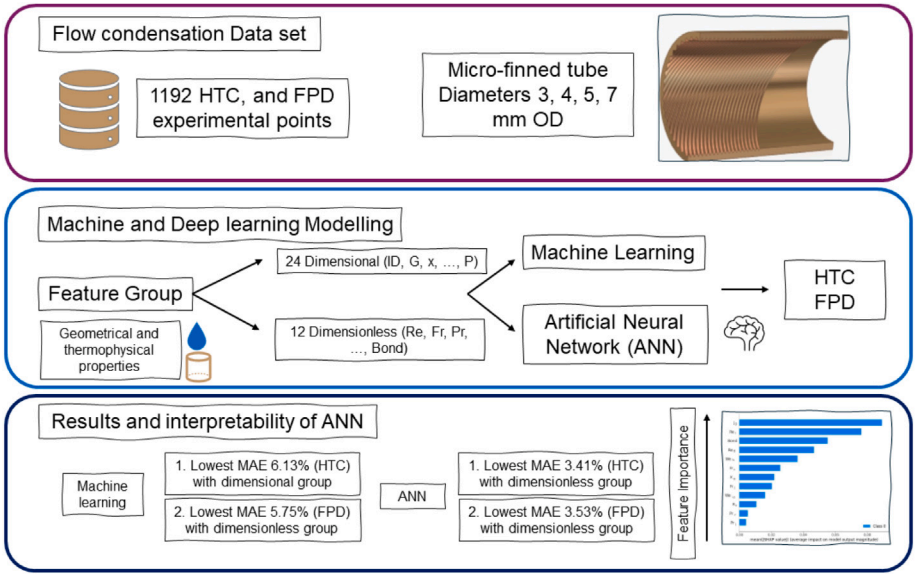

ARTICLE INFO

Keywords:
Condensation
Micro-finned tube
Artificial neural network
Machine learning
Deep learning

ABSTRACT

The design of micro-finned tube heat exchangers is a complex task due to intricate geometry, heat transfer goals, material selection, and manufacturing challenges. Nowadays, mathematical models provide valuable insights, aid in optimization, and allow us to explore various design parameters efficiently. However, existing empirical models often fall short in facilitating an optimal design because of their limited accuracy, sensitivity to assumption, and context dependency. In this scenario, the use of Machine and Deep Learning (ML and DL) methods can enhance accuracy, manage nonlinearity, adjust to varying conditions, decrease dependence on assumptions, automatically extract pertinent features, and provide scalability. Indeed, ML and DL techniques can derive valuable insights from datasets, contributing to a comprehensive understanding. By means of multiple ML and DL methods, this paper addresses the challenge of estimating key parameters in micro-finned tube heat exchangers such as the heat transfer coefficient (HTC) and frictional pressure drop (FPD). The methods have been trained and tested using an experimental dataset consisting of over a thousand data

* Corresponding author.
E-mail address: andrea.diani@unipd.it (A. Diani).
[1] Equal contribution and first authorship.

https://doi.org/10.1016/j.egyai.2024.100370
Received 23 November 2023; Received in revised form 5 March 2024; Accepted 16 April 2024
Available online 18 April 2024

points associated with flow condensation, involving various tube geometries. In this context, the Artificial Neural Network (ANN) demonstrates superior performance in accurately estimating parameters with MAEs in the range below 4.5% for both HTC and FPD. Finally, recognizing the importance of comprehending the internal mechanisms of the black-box ANN model, the paper explores its interpretability aspects.

Nomenclature

Artificial Intelligence.

Adaboost	Adaptive Boosting
AI	Artificial Intelligence
ANN	Artificial Neural Network
ANFIS	Adaptive Network-based Fuzzy Inference System
CI	Confidence Interval
CNN	Convolutional Neural Network
DL	Deep Learning
GB	Gradient Boosting
GRNN	Generalized Regression Neural Network
KNN	K-nearest Neighbor
MAE	Mean Average Error
ML	Machine Learning
MLP	Multilayer Perceptron
MSE	Mean Squared Error
RBFN	Radial Basis Function Network
RF	Random Forest
RFR	Random Forest Regression
RMSE	Root Mean Squared Error
SVR	Support Vector Regression
XGboost	Extreme Gradient Boost

Thermal.

Bond	Bond Number
c_p	Specific heat capacity, J kg^{-1} K^{-1}
D	Fin tip diameter, m
e	Fin height, m
EF	Enhancement factor
FPD	Frictional Pressure Drop (per unit length), Pa m^{-1}
Fr	Froude number
G	Mass flux, kg m^{-2} s^{-1}
GWP	Global Warming Potential
g	Gravity, 9.8 m s^{-2}
h	Fin height, m; specific enthalpy, J kg^{-1}
HC	HydroCarbon
HFC	HydroFluoroCarbon
HFO	HydroFlouoroOlefin
H_{lv}	Latent Heat of Vaporization, kJ kg^{-1}
HTC	Heat transfer coefficient, W m^{-2} K^{-1}
i	Uncertainty
ID	Inner diameter, m
J_g	Dimensionless gas velocity
OD	Outer diameter, m
n	Number of fins
Nu	Nusselt number
Pr	Prandtl
P	Pressure, bar
Re	Reynolds number
T	Temperature, ° C
U	Superficial velocity, m s^{-1}
X_{tt}	Martinelli parameter (Turbulent-Turbulent)
We	Weber number
x	Vapor quality

Greek symbols.

α, β	Helix angle, °
δ	Wall thickness, m
ΔT_{Sat}	Saturation and wall temperature difference, ° C
γ	Apex angle
λ	Thermal conductivity, W m^{-1} K^{-1}
μ	*Viscosity*, Pa · s
ρ	Density, kg m^{-3}
σ	Surface tension, N m^{-1}

Subscript.

g, v	Vapor phase
l	Liquid phase
sat	Saturation

1. Introduction

The design of heat exchangers which are omnipresent in energy systems has been highlighted in many literary works with emphasis on amelioration of sizing methods. Upgrades in design methods were only made possible by accruing experimental research that is conducted under various operating conditions. While thermal system configurations are comprised of multitudinous components, a particular focus has been adopted on two-phase flow inside horizontal tubes as the intricacies and complexities of such configuration demand a comprehensive experimental and numerical assessment. In the aftermath of such scientific endeavors, many empirical correlations were introduced for thermal and hydraulic performance during boiling and condensation with the capability to produce fairly accurate values for heat transfer coefficient (HTC) and frictional pressure drop (FPD). With a specific focus on refrigerants, as they possess diverse thermophysical properties, exemplary empirical correlations [1–5] for flow condensation can be found in abundance whose validation has been carried out on HydroFluoroCarbons (HFCs) and recently for HydroFlouroOlefines (HFOs) with minimized climate change contributions through their exceptionally low GWP. A shared aspect among noted correlations is their reliance on experimentally acquired data points. To detach the correlation's dependence from testing conditions thus building a generalized equation, most equations are based on dimensionless parameters, a list of which prevalently used is included in Table 1. Regarding the precision of stated correlations, in a holistic literature review, Zhang et al. [6], garnering experimental data and comparing the accuracy of promising empirical models, put forward that among the entirety of the collected database, the most accurate model being the model by Cavallini et al. [1], had a mean absolute error (MAE) of 17%. Regarding mini-scale geometries and conventional ones, the fairest predictions were made with an MAE of 20.6% and 14.4% respectively. Furthermore,

Table 1
Parameters and expressions.

Parameter	Expression
Bond number Bo	$\frac{g(\rho_l-\rho_v)D^2}{\sigma}$
Martinelli parameter X_{tt}	$\left(\frac{1-x}{x}\right)^{0.9}\left(\frac{\rho_v}{\rho_l}\right)^{0.5}\left(\frac{\mu_l}{\mu_v}\right)^{0.1}$
Reynolds number Re_l	$(1-x)\frac{GD}{\mu_l}$
Reynolds number Re_v	$x\frac{GD}{\mu_v}$
Prandtl number Pr_v	$\frac{c_{pv}\mu_v}{\lambda_v}$
Weber number We_{ls}	$\frac{\rho_l U_{ls}^2 D}{\sigma}$
Weber number We_{vs}	$\frac{\rho_v U_{vs}^2 D}{\sigma}$
Froude number Fr_l	$\frac{G(1-x)^2}{\rho_l^2 gD}$
Froude number Fr_v	$\frac{Gx^2}{\rho_v^2 gD}$
Non-dimensional vapor velocity J_g	$\frac{xG}{\left(gD\rho_v(\rho_l-\rho_v)\right)^{0.5}}$
Nusselt number Nu	$\frac{\mathrm{HTC}\cdot D}{\lambda_l}$

the authors rightfully expressed the need to construct models with acceptable accuracy for a broad range of testing conditions. Similar review attempts were conducted for correlations of frictional pressure drop as the paper of Kim and Mudawar [7] in which the average range of predictions made by models for condensation under various conditions exceeds 20% MAE. Delving into the accuracy of models concerning micro-finned tubes for climate-friendly refrigerants from the HFOs family one could refer to [8,9] where models with optimal precision recorded MAEs of 8.5% and 13.6% for HTC and FPD respectively. Since the geometrical parameters involved in finned surfaces are quite more complex than the conventional ones, contributing to the heterogeneity of structural arrangements, Li et al. [10] carried out a series of experiments on condensation inside five micro-fin tubes with diverse geometrical characteristics. Having concluded the comparison of recorded HTC and FPD for micro-fin tubes and empirical models, a high discrepancy of MAE was reported between the cases. Such variability is even more deplorable as a single model suffers from large differences in MAE with a change in the physical parameters of the micro-fin tube. For instance, regarding HTC, the previously mentioned model by [3] experiences MAE variability ranging from 4.2% to as high as 44.54% with alterations in helix angle, apex angle, fin height, and the number of fins along the circumference.

As evidence suggests, an optimal design of a heat exchanger whose imperativeness is elevating in the contemporary era, may not be satisfied by empirical models that could suffer from large deviations. With recent advancements in applications of Machine Learning (ML) and Deep Learning (DL) in heat exchangers that can be found in the open literature [11], discovering more precise causal links in intricate underlying patterns among the abovementioned geometrical and thermophysical parameters, heat transfer coefficient, and frictional pressure drop characteristics has been made possible. Table 2 offers a succinct review of the utilization of ML for the prognostication of heat transfer coefficient and frictional pressure drop during two-phase flow. It must be noted that both dimensional and dimensionless parameters were used in the ML assessments of HTC and FPD.

In an assessment of Table 2:

- One could notice the absence of ML and DL implementation for data points concerning flow condensation inside micro-fin tubes.
- A reprehensible aspect in the utilization of ML and DL could be related to the existence of only a few attempts to build interpretable models for estimations of HTC and FPD.
- It is plausible to draw an inference that although the collection of experimental points from literature elevates the quantity of data points therefore enriching the assessment, the immutable discrepancies between testing facilities and the associated experimental uncertainties could play a role in the distortion of the learning process of the models.
- While some articles are dedicated to dimensionless features and some to dimensional ones, none of which is dedicated to drawing a comparison as to how the outcome could differ for the two cases
- A holistic approach that encompasses a wide range of ML models is lacking in the assessments of the authors.

To address such shortcomings in the prediction of HTC and FPD, the following paper garners and implements ML and DL methods on 1192 data points of flow condensation inside micro-finned tubes, all of which were collected at the Heat Transfer MicroGeometries laboratory of the University of Padova. Having considered copious numbers of ML and DL models for two categories of features, a selection of which most capable of producing accurate results is then considered and provided. Furthermore, DL models were scrutinized on the basis of their interpretability to highlight salient input parameters that share most of the impact of the resulting HTC and FPD.

2. Experimental database

The data points implemented for training, validation, and testing purposes are comprised of a wide range of low-GWP refrigerants (pure and azeotropic mixture) under four geometrically diverse micro-finned tubes. Table 3 is constructed to delineate the experimental conditions of the data points. As demonstrated, the only data set not already published in the literature is with regard to condensation of R515B whose experimental methodology can be found in the addendum.

The geometrical properties present in Table 3 are demonstrated by circumferential and peripheral perspectives that are present in Figs. 1 and 2.

3. Methodology

3.1. Input features

As previously mentioned, two categories of features are implemented for the prediction process namely dimensional and dimensionless groups. The expressions are provided as:

Dimensional features:

$$f(ID, n, h, \beta, \gamma, P, G, x, \Delta T, U_l, U_v, P_{\mathrm{red}}, T_{\mathrm{sat}}, \rho_l, \rho_v, \mu_l, \mu_v, \lambda_l, \lambda_v, \sigma, c_{p_l}, c_{p_v}, H_{lv}) = \mathrm{HTC},\ \mathrm{FPD} \quad (1)$$

where H_{lv} is the latent heat of vaporization.

Dimensionless features:

$$f(\mathrm{R_x}, \mathrm{X_{tt}}, \mathrm{Re_l}, \mathrm{Re_g}, \mathrm{Pr_l}, \mathrm{Pr_v}, \mathrm{We_{ls}}, \mathrm{We_{vs}}, \mathrm{F_{rl}}, \mathrm{F_{rv}}, \mathrm{J_g}, \mathrm{Bond}) = \mathrm{HTC}, \mathrm{FPD} \quad (2)$$

It must be noted that three of the dimensional inputs present in equation 1, namely reduced pressure (P_{red}), superficial liquid velocity (U_l), and superficial vapor velocity (U_v), are functions of other dimensional parameters and the premise behind their implementation is their imperative nature in the assessment of two-phase flow. Parameter (R_x) in Eq. (2) was initially suggested by [3] as the heat transfer area of a micro-finned tube compared to that of the smooth tube with an identical inner diameter (*ID*). Such expression assists in a dimensionless expression of geometrical parameters of the micro-finned tubes. Although expressions of Nusselt number (Nu) and two-phase multiplier are common in dimensionless models of heat transfer coefficient and pressure drop, in training of the ML and DL models the output has been assumed to be dimensional parameters of HTC and FPD. To further elucidate the causality for which such a decision was made, one could refer to expressions of Nu and two-phase multiplier.

Table 2
Summary of authors, database, ML methods, and results.

Reference	Database Details	Method Used	Results
Nie et al. [12]	6054 data points (HFCs, HFOs, CO2, ammonia) (0.49-8.92 mm ID)	KNN, RF, XGBoost, ANN, CNN	1. Best HTC MAE of 5.82% achieved by the CNN method on testing data points of 1213. 2. Universal HTC correlation created with an accuracy of 19.21% MAE over the entire database.
Azizi and Ahmadloo [13]	440 data points (R134a, 8.38 mm ID, various inclinations)	MLP network	1. MAE 1.94% for tested data. 2. 18 neurons in the hidden layer proven to be the most suitable with the lowest MAD.
Balcilar et al. [14]	368 data points by experimentation (R134a, Vertical 8.1 mm ID)	ANN, MLP, RBFN, GRNN, ANFIS	1. Methods of MLP and RBFN proven to be most accurate for both FPD and HTC in the range of ±5% MAE.
Mattiuzzo et al. [15]	1504 data points by experimentation (R513A, R516A, Horizontal 3.38, 0.98 mm ID)	ANN Matlab toolbox	1. MAE of below 6.3%. 2. The number of hidden neurons surpassing the value of 12 does not substantially affect the predictive model.
Tarabkhah et al. [16]	348 data points (R134a, R1234yf, Inclined, 8.3 mm ID)	MLP, SVR, XGBoost, KNN	1. MLP and XGboost possess the most optimal prediction for HTC and FPD respectively.
Hughes et al. [17]	1032 data points (Ethane/propane, R245fa/pentane, 410A, 0.76-14.45 mm D_h channels)	SVR, RFR, GB, ANN	1. SVR model and GB with predictions within 5 and 5.5% MAEs for Nu and FPD respectively. 2. Highest importance factor of the Bond number on the FPD.
Zhou et al. [18]	4882 data points (HFCs, HFOs, HCs, CO2, 0.424-6.52 mm D_h)	ANN,RF, AdaBoost, XGBoost	1. ANN and XGBoost provided the best HTC results with MAD of 6.8% and 9.1%. 2. ANN and XGBoost are superior to developed empirical methods.
Lin et al. [19]	7349 data points (HFCs, HFOs, CO2, 3.64–11.98 mm ID, $11° < \beta < 50°$, $6° < \gamma < 30°$, $0.11 < e < 0.26$ mm)	Dimnet	1. Interpretable ML model allows the construction of a universal model for flow boiling with MAEs between 5% and 20% for vapor qualities lower than 0.7 and mass fluxes lower than 800 kg m^{-2} s^{-1}.

Table 3
Summary of experimental data.

Data	Test conditions	Geometrical characteristic	Number of data points	Mean experimental uncertainty (CI95%)
Diani et al [9]	G = 50–400 kg m^{-2} s^{-1}, T_{sat} = 30°C, 40°C R515B R1234ze(E)	6.14 mm ID, β = 18°, e = 0.18 mm	237	5%
Appendix A.1	G = 75–600 kg m^{-2} s^{-1}, T_{sat} = 30°C, 40°C R515B	4.28 mm ID, β = 30°, e = 0.15 mm	102	3.4%
Irannezhad et al. [20]	G = 75–600 kg m^{-2} s^{-1}, T_{sat} = 30°C, 40°C R1234ze(E)	4.28 mm ID, β = 30°, e = 0.15 mm	103	3.4%
Diani et al. [21]	G = 100–1000 kg m^{-2} s^{-1}, T_{sat} = 30°C, 40°C R513A	3.4 mm ID, β = 18°, e = 0.12 mm	117	4%
Diani et al. [22]	G = 100–1000 kg m^{-2} s^{-1}, T_{sat} = 30°C, 40°C R1234ze(E) R134a	3.4 mm ID, β = 18°, e = 0.12 mm	249	4.2%
Diani et al. [8]	G = 100–1000 kg m^{-2} s^{-1}, T_{sat} = 30°C, 40°C R1234yf	3.4 mm ID, β = 18°, e = 0.12 mm	103	2.4%
Diani et al. [23]	G = 100–1000 kg m^{-2} s^{-1}, T_{sat} = 30°C, 40°C R513A	2.4 mm ID, β = 7°, e = 0.12 mm	98	4.2%
Diani et al. [24]	G = 250–1000 kg m^{2} s^{-1}, T_{sat} = 30°C, 40°C R1234ze(E) R1234yf R134a	2.4 mm ID , β = 7°, e = 0.12 mm	183	2.4%
Total Data Points = 1192				

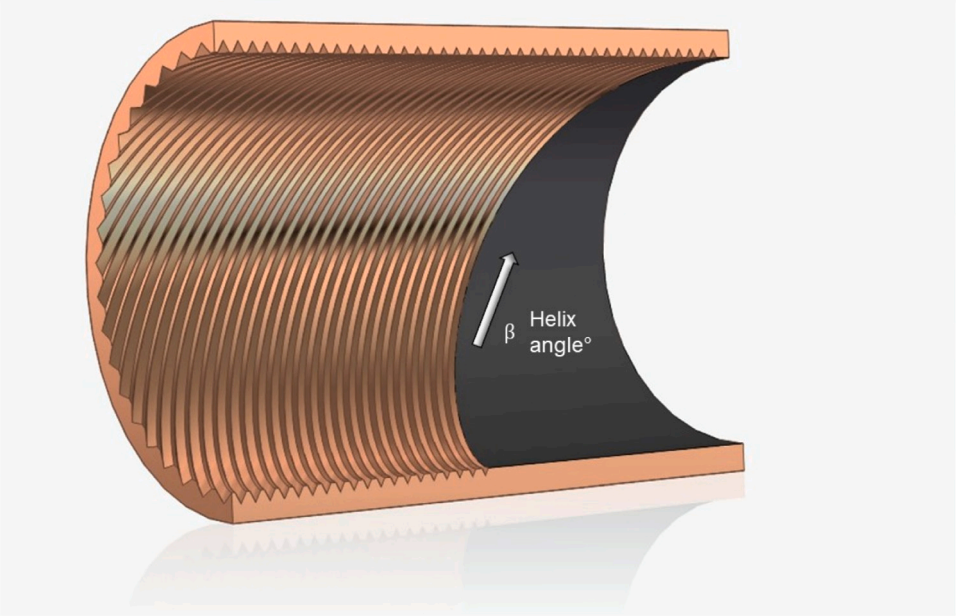

Fig. 1. Peripheral view of the micro-finned tube.

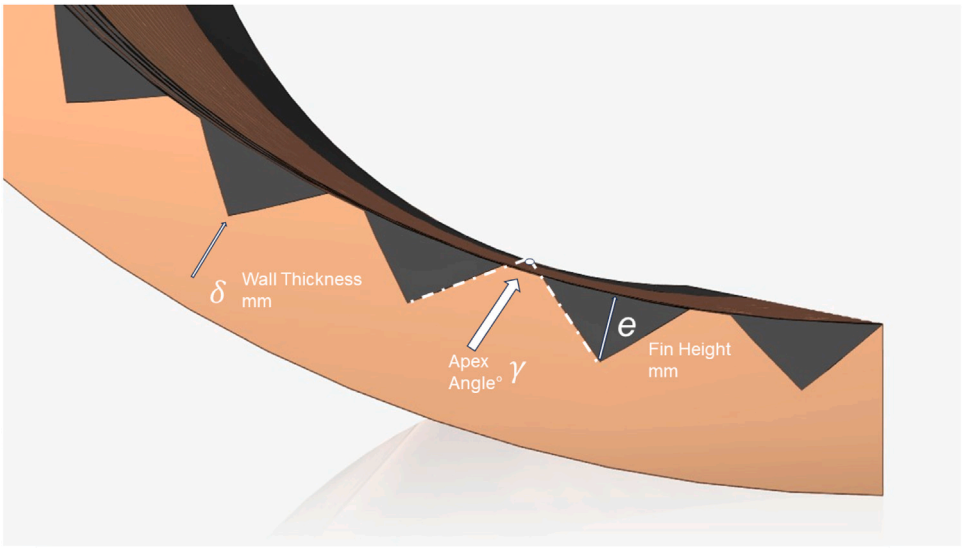

Fig. 2. Circumferential view of the micro-finned tube.

- The equation for HTC:

$$\mathrm{HTC} = \frac{\mathrm{Nu} \cdot \lambda}{D} \tag{3}$$

where Nu is commonly expressed as:

$$\mathrm{Nu} = f(\mathrm{Pr}, \mathrm{Re}, \ldots) \tag{4}$$

- The equation for two-phase ΔP:

$$\frac{\Delta P_{\text{Two-Phase}}}{L} = \left(\Phi_v^2\right) \cdot \frac{\Delta P_{\text{Single-Phase,v}}}{L} \tag{5}$$

Where Φ_v is commonly expressed as:

$$\Phi_v = f(X_{tt}, \ldots) \tag{6}$$

As evident, the relationship between Nusselt and HTC will not be severely affected, unless large variations of thermal conductivity and inner diameter are experienced, and the database under study does not present such large variations and the same also applies to the two-phase multiplier. Furthermore, in a trial run, the Nusselt number and two-phase multiplier were assumed to be the function of dimensionless inputs in Eq. (2), and quite low accuracy was reported during testing. As a result, it was assumed that in ML and DL assessment the learning process is considerably better using HTC and FPD values as the output.

3.2 Data preprocessing

Our dataset contains 1192 data points divided into two separate datasets: one with 25 features representing dimensional data and the other with 14 features representing non-dimensional data. We use a dual-track approach to conduct comprehensive experiments, treating these datasets independently. We began the preprocessing phase by addressing missing values to ensure data integrity. Only one row displayed this characteristic, which was then removed, resulting in a clean dataset. Following that, we used the Standard Scaler transformation,

which uses the mean and standard deviation of the input data to scale each feature in order to normalize the input data and ensure that each feature contributes equally to the learning process. Normalization aims to standardize all features, preventing certain features from dominating the learning process due to their higher numerical values. This step is critical for gradient-based optimization methods and other algorithms that are sensitive to the scale of input features. Following that, we divided our dataset into training and testing sets. 70% of the data in this division is designated for training, while the remaining 30% is designated for testing and validation. The thorough preprocessing procedures we followed ensured a solid and trustworthy analysis of the datasets, which enhanced the validity and trustworthiness of our conclusions.

3.3 Machine and deep learning models

In this section, we delve into the ML and DL models employed to tackle the regression task at hand. As previously mentioned, our approach encompasses a diverse array of models, ensuring a comprehensive exploration of the problem space. However, it is noteworthy to mention that, despite the potential benefits of utilizing metaheuristic optimization algorithms such as Simulated Annealing [25], Genetic Algorithm [26], Particle Swarm Optimization [27], Grey Wolf Optimization [28], and Golden Search Optimization [29], we have consciously chosen not to incorporate them for the purpose of model comparison, avoiding unnecessary complexity and enabling a focused evaluation of each model's inherent capabilities. The multifarious techniques employed are provided as:

- **Linear Regression** [30]**:** To establish relationships between the input features and the target variable, a basic linear modeling technique is used.
- **XGBoost** [31]**:** XGBoost provides an ensemble learning framework that can handle complex relationships in the data by utilizing the power of gradient boosting. XGBoost stands out as a promising and effective tool for applications in the energy sector, characterized by its exceptional precision, efficiency, and stability [32].
- **KNN** [33]**:** By taking into account the average of its k-nearest neighbors in the feature space, a regression model based on k-nearest neighbors predicts the target variable.
- **Decision Tree** [34]**:** The model partitions the feature space into regions and assigns a constant value to each region in decision tree-based regression.
- **Random Forest** [35]**:** An ensemble technique for improving accuracy and robustness by constructing multiple decision trees and combining their predictions. The number of estimators parameter is the number of trees in the forest. In our implementation, we set this parameter to 100.
- **LightGBM** [36]**:** LightGBM is an efficient gradient boosting framework that uses tree-based learning algorithms and excels at handling large datasets. In our LightGBM implementation, we tailored several critical parameters to enhance model performance: number of leaves (31), governing tree complexity; learning rate (0.05), modulating step size for training convergence; feature fraction (0.9), orchestrating feature randomness; bagging fraction (0.8), instigating data randomness; and bagging frequency (5), determining the frequency of data bagging during training.
- **SVR (Support Vector Regression):** SVR is capable of capturing complex relationships in high-dimensional spaces by utilizing the principles of support vector machines. We configured two key parameters to influence the model behavior in our SVR implementation: kernel 'linear' which specifies the type of kernel function used, and C (1.0), which controls the regularization strength.
- **Ridge Regression** [37] **:** By penalizing large coefficients, a linear regression technique with an added regularization term helps to prevent overfitting.
- **Elastic Net** [38] **:** By combining the best features of Lasso and Ridge regression, Elastic Net is a powerful statistical technique that effectively addresses multicollinearity and variable selection issues in the predictive modeling process.
- **Polynomial Regression** [39]**:** By incorporating polynomial features into linear regression, non-linear relationships between variables can be explored. In our implementation, we changed the critical parameter degree (2), which allows us to vary the degree of the polynomial features generated by the Polynomial Features function.
- **RANSAC Regressor** [40]**:** Random Sample Consensus (RANSAC) is an iterative algorithm robust to outliers, particularly suitable for datasets with noisy observations.
- **Deep Learning Model (Artificial Neural Network):** Our feed-forward architecture deep learning regression model leverages the expressive power of artificial neural networks to extract complex patterns from the data. We recognize the unique qualities of predicting HTC and FPD as target features in our study. We have chosen a customized approach because we recognize that these two aspects of the regression task might benefit from distinct neural network architectures. We discovered that the best way to predict HTC and FPD is to use two separate neural network models, each tailored to the specific needs of its target feature. This requires adjusting hyperparameters such as the number of hidden layers and neurons within these layers. This approach allows each model to specialize in capturing the distinct patterns and relationships associated with either HTC or FPD. We hope to improve the models' ability to discern and represent the complexities of the respective output variables by fine-tuning the architecture for each prediction task. The architecture and hyperparameters employed in our models are detailed in Table 4. We incorporated Rectified Linear Unit (ReLU) activation layers in both neural networks to introduce non-linearity and enhance the model's capacity to capture complex patterns. Additionally, the Adam optimization algorithm was employed during the training process. A relatively low learning rate was chosen to prevent overfitting, particularly in complex models with multiple hidden layers. The model can gradually converge with a low learning rate, reducing the risk of overshooting optimal weights and preventing oscillations around the minima. Furthermore, using a large enough number of epochs allows the model to learn from the entire training dataset, capturing intricate patterns while avoiding overfitting. Furthermore, we closely monitored the model's performance during training on a dedicated validation set to avoid overfitting. We employed the mean squared error as the loss function for training both neural networks.

4 Evaluation and results

In the evaluation phase, we assess the performance of our ML and DL models using key metrics: Mean Absolute Error (MAE), Mean Squared Error (MSE), Root Mean Squared Error (RMSE), and R-squared (R^2). The formulas for these metrics are defined as follows:

$$\mathrm{MAE} = \frac{1}{n}\sum_{i=1}^{n}\left|y_i - \hat{y}_i\right| \tag{7}$$

$$\mathrm{MSE} = \frac{1}{n}\sum_{i=1}^{n}(y_i - \hat{y}_i)^2 \tag{8}$$

$$\mathrm{RMSE} = \sqrt{\mathrm{MSE}} \tag{9}$$

$$R^2 = 1 - \frac{\sum_{i=1}^{n}(y_i - \hat{y}_i)^2}{\sum_{i=1}^{n}(y_i - \bar{y})^2} \tag{10}$$

Although it is customary in ML and DL to express MAE in the same unit as the target variable, the unitless expression of such metrics is

Table 4
Neural network architecture and hyperparameters for HTC and FPD prediction.

Target	Architecture	Layers	Batch size	Learning rate	Number of epochs
HTC	Feed-forward Neural Network	3 (512, 256, 1)	32	0.0005	400
FPD	Feed-forward Neural Network	4 (1028, 512, 256, 1)	128	0.0005	450

Table 5
Performance Metrics for HTC prediction using dimensional data.

Method	MAE[a]	MSE[a]	RMSE[a]	R^2	MAE %
Linear Regression	1.14	2.56	1.60	0.87	13.52%
XGBoost	0.55	0.60	0.77	0.97	6.55%
KNN	0.81	1.34	1.16	0.93	9.60%
Decision Tree	0.84	1.65	1.28	0.92	9.98%
Random Forest	0.55	0.68	0.83	0.96	6.60%
LightGBM	0.54	0.70	0.83	0.96	6.47%
SVR	1.11	3.07	1.75	0.85	13.22%
Ridge Regression	1.19	2.71	1.64	0.86	14.14%
Polynomial Regression	0.61	0.90	0.95	0.95	7.23%
Elastic Net	1.76	5.50	2.34	0.73	20.88%
RANSAC Regressor	0.86	0.90	0.95	0.77	13.03%
Artificial Neural Network	0.28	0.19	0.44	0.99	3.41%

[a] ($kW/(m^2\ K)$)

Table 6
Performance Metrics for FPD per unit of length prediction using dimensional data.

Method	MAE[a]	MSE[a]	RMSE[a]	R^2	MAE %
Linear Regression	0.05	0.004	0.07	0.91	29.03%
XGBoost	0.013	0.0007	0.027	0.98	7.23%
KNN	0.034	0.0035	0.059	0.94	18.89%
Decision Tree	0.021	0.0019	0.044	0.96	11.88%
Random Forest	0.013	0.0006	0.026	0.98	7.46%
LightGBM	0.013	0.0007	0.026	0.98	7.51%
SVR	0.059	0.0053	0.073	0.90	32.33%
Ridge Regression	0.054	0.0050	0.071	0.91	29.89%
Polynomial Regression	0.010	0.0002	0.015	0.99	5.75%
Elastic Net	0.19	0.060	0.24	0	107.20%
RANSAC Regressor	0.05	0.0061	0.078	0.89	27.73%
Artificial Neural Network	0.0064	0.0001	0.010	0.99	3.53%

[a] (bar/m)

prevalently expressed in the field of thermal sciences to detach the results from the unit of measurement, providing a better grasp of model's accuracy. In this case, the evaluation contains reports of absolute and percentage-based metrics. The percentage-based evaluation metric is calculated as follows:

$$\text{MAE Percentage} = \left(\frac{\text{MAE}}{\text{Mean actual Values}}\right) \times 100 \tag{11}$$

Percentage-based metrics provide a normalized measure of error, making them particularly useful for comparing models across different target variables. After training each of the previously mentioned models, we proceed to evaluate their performance based on the selected metrics.

4.1 Evaluation of dimensional data

Although building predictive models by dimensional values is scarce in empirical attempts, delving into the possibility of the construction of ML and DL models based on these inputs is of high importance. In this section, we undertake the evaluation of our dimensional dataset characterized by the presence of 23 features for training and two target features. The results of the evaluation for the prediction of HTC and FPD are succinctly presented in Tables 5 and 6.

Based on a comprehensive evaluation of performance metrics, XGBoost, Random Forest, LightGBM, and Polynomial Regression outperform other ML models in terms of predictive efficacy for HTC. The ANN also distinguishes itself by displaying the models with the lowest error values. In comparison to the aforementioned algorithms, Elastic Net and RANSAC Regressor exhibit relatively higher error metrics, indicating their limited effectiveness in modeling the complex patterns inherent in the dataset. Furthermore, the consistently high R^2 values across most methods highlight the significant proportion of HTC variance effectively explained by XGBoost, Random Forest, LightGBM, Polynomial Regression, and ANN, solidifying their position as robust models for HTC prediction in comparison to alternative approaches. The prediction plots for the top models are shown in Fig. 3. Plots for other models will also be included in the annex.

In a parallel evaluation, XGBoost, Random Forest, Polynomial Regression, and LightGBM consistently outperformed other algorithms in predicting FPD. Despite this, the ANN exhibited the lowest error values, showcasing its robust predictive capabilities. This consistency across tasks underscores the adaptability and reliability of ANN, Random Forest, LightGBM, Polynomial Regression, and XGBoost for dimensional data predictive modeling. Refer to Fig. 4 for prediction plots of the top models.

Table 7
Performance Metrics for HTC prediction using non-dimensional data.

Method	MAE[a]	MSE[a]	RMSE[a]	R^2	MAE %
Linear Regression	1.35	3.69	1.92	0.82	15.86%
XGBoost	0.52	0.61	0.78	0.97	6.13%
KNN	0.98	2.08	1.44	0.90	11.48%
Decision Tree	0.94	1.86	1.36	0.91	11.00%
Random Forest	0.64	0.85	0.92	0.95	7.51%
LightGBM	0.54	0.63	0.79	0.96	6.47%
SVR	1.31	4.26	2.06	0.79	15.30%
Ridge Regression	1.35	3.71	1.92	0.82	15.87%
Polynomial Regression	0.97	1.63	1.27	0.92	11.44%
Elastic Net	2.02	7.62	2.76	0.63	23.63%
RANSAC Regressor	1.29	3.8	1.97	0.81	15.09%
Artificial Neural Network	0.34	0.28	0.53	0.98	4.02%
Empirical model [3]	1.66	6.92	2.63	0.66	19.46%

[a] ($kW/(m^2K)$)

4.2 Evaluation of non-dimensional data

This section deals with the assessment of our non-dimensional dataset that has two target features and twelve training features. Tables 7 and 8 provide a concise presentation of the evaluation results for the prediction of HTC and FPD.

Regarding HTC prediction with non-dimensional data, the performance metrics table offers useful information about model effectiveness. As before, XGBoost, Random Forest, and LightGBM exhibit better accuracy with smaller error values when compared to other models. Reiterating its strong predictive capabilities, the ANN stands out with the lowest error values. These results show that the algorithms retain their relative performance trends between the two datasets when compared to the table for HTC prediction using dimensional data that was previously discussed. The detailed comparison and implications of these findings will be explored further in the discussion section. Furthermore, most models demonstrate superior accuracy to that of the empirical model by Cavallini et al. [3] which was considered a candidate for comparative analysis owing to its promising fairly accurate predictions which are present in the open literature. It is pivotal to clarify that the dimensionless groups of [3] although close, are not entirely similar to the ones utilized by ML models.

XGBoost, Random Forest, Polynomial Regression, and LightGBM demonstrate superior accuracy in FPD prediction, which is consistent with the trends observed in HTC prediction tasks. Furthermore, ANN stands out with low error values, highlighting its robust predictive performance. The detailed comparative analysis and implications of these

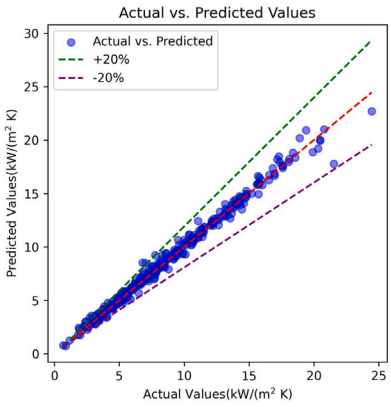

(a) HTC prediction of ANN model

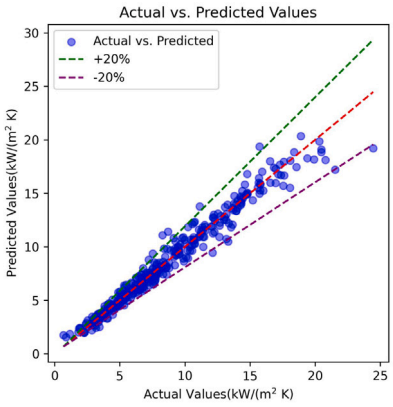

(b) HTC prediction of LightGBM

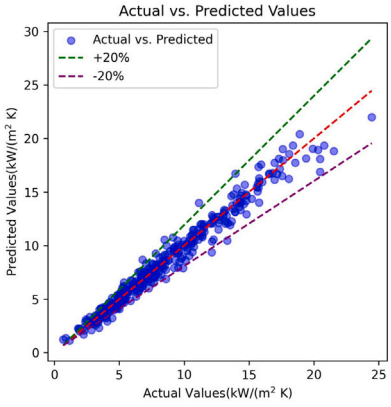

(c) HTC prediction of XGBoost

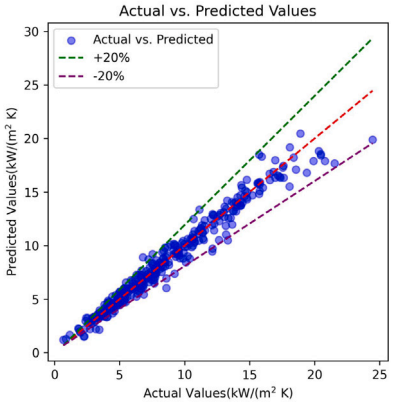

(d) HTC prediction of Random Forest

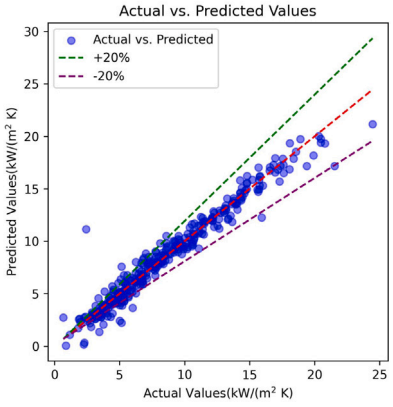

(e) HTC prediction of Polynomial Regression

Fig. 3. HTC prediction using dimensional data.

findings will be expounded upon in the subsequent discussion section. Furthermore, the empirical model of Diani et al. [41] which was built on the micro-finned tube of 3.4 mm ID with identical geometrical properties to that of the included database is provided among the ML and DL models (see Fig. 6).

4.3 Interpretability

The ability to interpret ML and DL models is critical for gaining insights into their decision-making processes. Despite the importance of interpretability, only a small number of research papers address it. While many consider DL models to be the best, their inherent black-box nature frequently steers researchers toward more interpretable models such as decision trees for analysis.

In our study, we recognize the importance of interpretability and opt to employ the SHAP (SHapley Additive exPlanations) library [42]. In the subject of explainable AI, SHAP is highly esteemed for its capacity to offer lucid insights into model predictions. It provides a strong framework for deciphering complex models by utilizing Shapley values from cooperative game theory to assign the contributions of each feature to the prediction outcome. In particular, we use the SHAP library's Deep Explainer to interpret the output from our top-performing model, the ANN. The Deep Explainer is designed for DL models, making it an excellent choice for deciphering the complexities

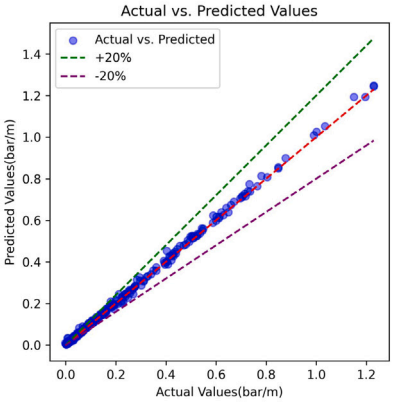

(a) FPD prediction of ANN model

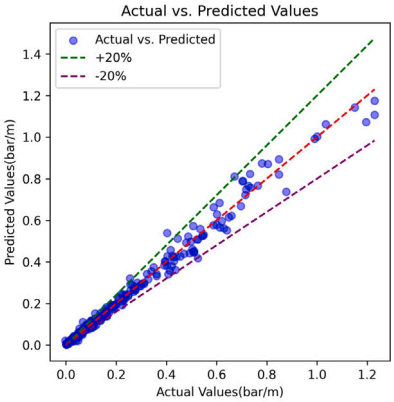

(b) FPD prediction of LightGBM

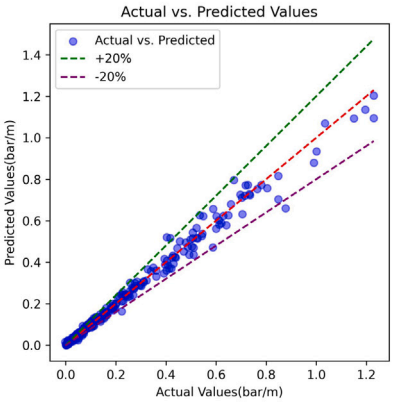

(c) FPD prediction of XGBoost

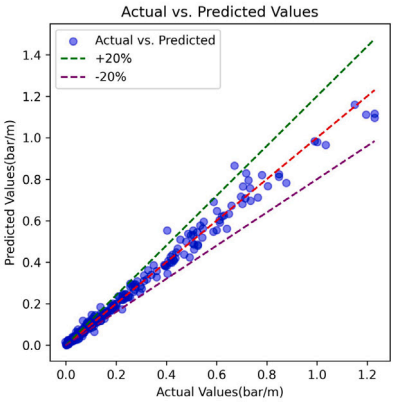

(d) FPD prediction of Random Forest

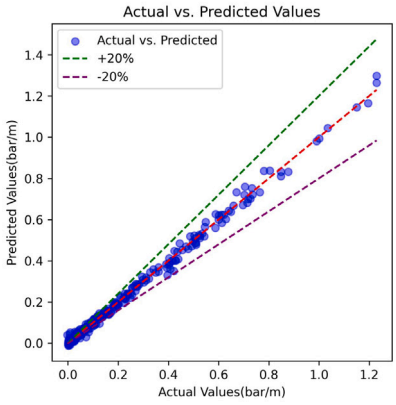

(e) FPD prediction of Polynomial Regression

Fig. 4. FPD per unit of length prediction using dimensional data.

of ANNs. This method allows us to decipher the black-box nature of our ANN model and shed light on the factors that influence its predictions. Figs. 7, 8, 9, 10 depict the average impact of each feature on the model's output, allowing for a visual representation of the interpretability results. Moreover, the delineation of SHAP values and delving into the magnitude of the impact of one feature relative to others will provide a novel assessment of two-phase flow. Such aspect is quite evident from the scrutinization of literary works in flow condensation where prioritization in the contribution of geometrical or thermophysical properties provides a great insight into heat transfer and hydraulic performance during condensation inside micro-finned tubes. A thorough analysis of the acquired results of SHAP values and their implications for the flow condensation models are given in the thermal perspective of the discussion section. It is worth noting that there exists an extension of the Shapley values known as Asymmetric Shapley Values (ASVs) [43], which offer users the ability to integrate partial causal knowledge into the explanation process. ASVs represent a significant advancement in the field of explainable AI, as they enable a more nuanced understanding of causal relationships within complex systems. For further insights into this method and its implications, interested readers are encouraged to explore the Future Work section, where additional information about ASVs will be provided.

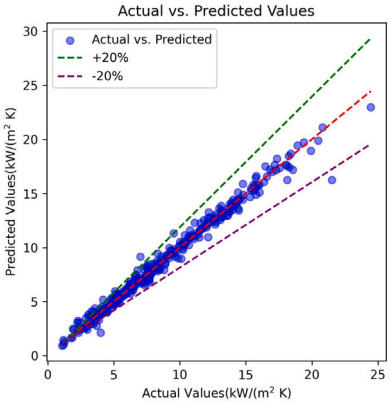

(a) HTC prediction of ANN model

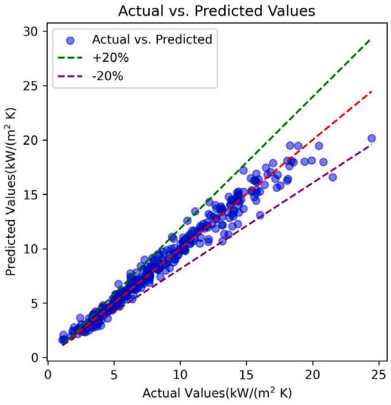

(b) HTC prediction of LightGBM

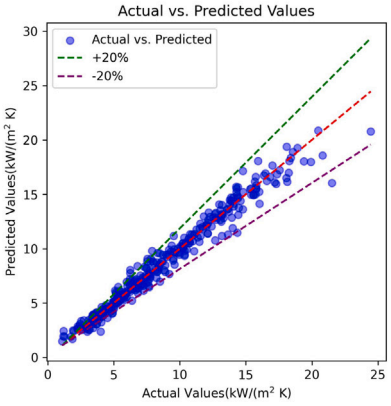

(c) HTC prediction of XGBoost

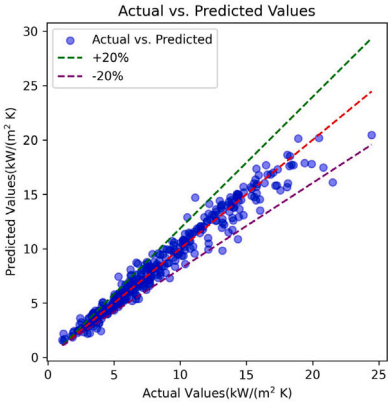

(d) HTC prediction of Random Forest

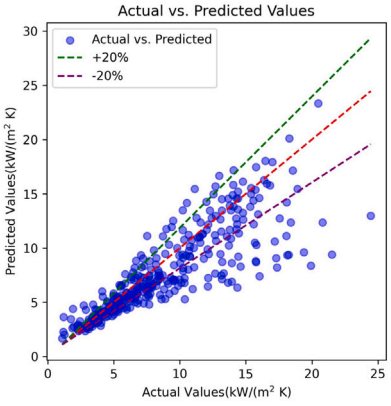

(e) HTC prediction of Empirical Model

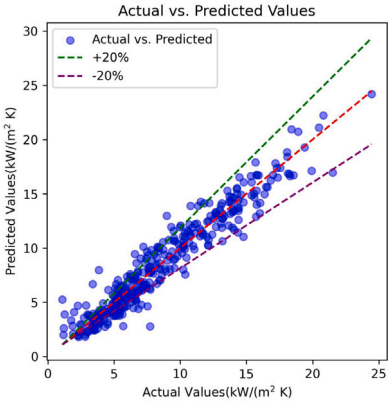

(f) HTC prediction of Polynomial Regression

Fig. 5. HTC prediction using non-dimensional data.

5 Discussion

The presented study investigates the predictive performance of various ML and DL models in two distinct tasks: HTC and FPD prediction. The analysis considers both dimensional and non-dimensional data to glean insights into the models' adaptability and efficacy. Also, the examination seeks to identify whether one type of data yields superior performance compared to the other.

5.1 AI perspective

5.1.1 HTC prediction: Dimensional vs. Non-dimensional data

The comparison of dimensional and non-dimensional data in the context of HTC prediction reveals intriguing patterns. Notably, XGBoost, Random Forest, LightGBM, and ANN consistently outperform in both datasets, indicating their robustness across data types. In both scenarios, the ANN performs admirably in terms of prediction. Almost all of the models show noticeable changes when switching from

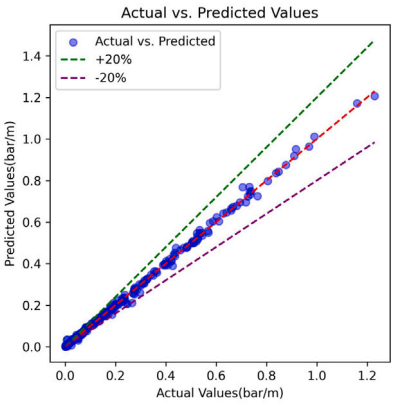

(a) FPD prediction of ANN model

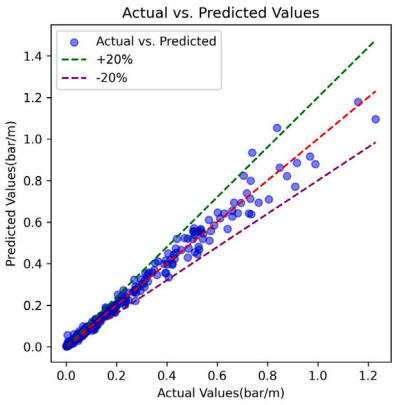

(b) FPD prediction of LightGBM

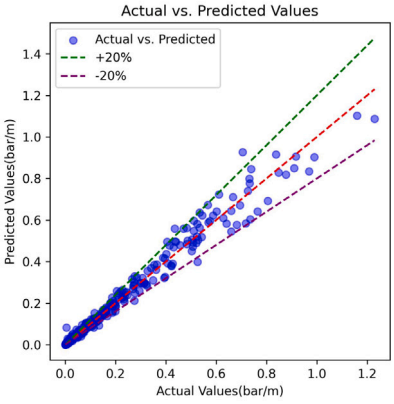

(c) FPD prediction of XGBoost

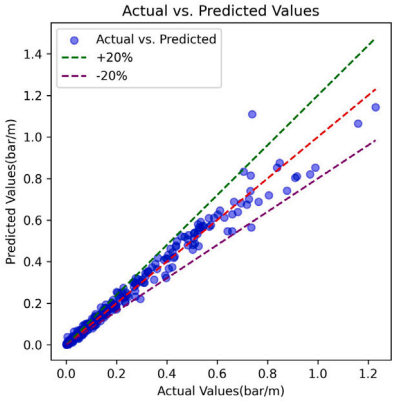

(d) FPD prediction of Random Forest

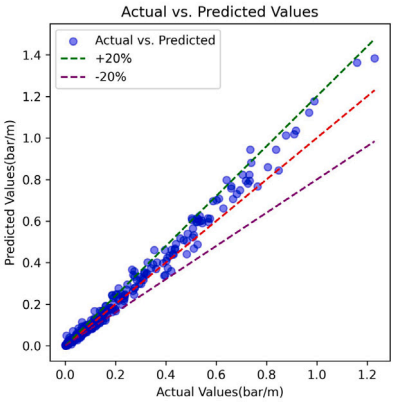

(e) FPD prediction of Empirical model

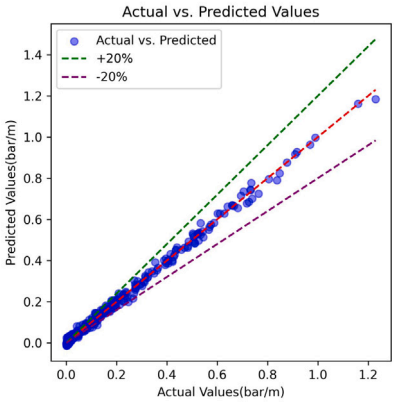

(f) FPD prediction of Polynomial Regression

Fig. 6. FPD per unit of length prediction using non-dimensional data.

dimensional to non-dimensional data, as evidenced by an increase in error metrics. Linear Regression, Elastic Net, and Support Vector Regression (SVR), for example, exhibit sensitivity to data transformation, as evidenced by an increase in error values. On the other hand, in the non-dimensional setting, XGBoost, LightGBM, and ANN show consistent or slight variations in their performance. This resilience highlights the algorithms' ability to adjust to the intrinsic properties of the data, highlighting their efficacy in a variety of representations. As a benchmark, the HTC prediction using non-dimensional data is compared to the empirical model. The empirical model is consistently outperformed by the majority of the ML and DL models (11 out of 12), demonstrating the efficacy of advanced modeling techniques in capturing complex relationships within the data.

5.1.2 FPD prediction: Dimensional vs. Non-dimensional data

XGBoost, Random Forest, LightGBM, Polynomial Regression, and ANN dominate FPD prediction in both dimensional and non-dimensional datasets, as they do in HTC prediction. Once again, the

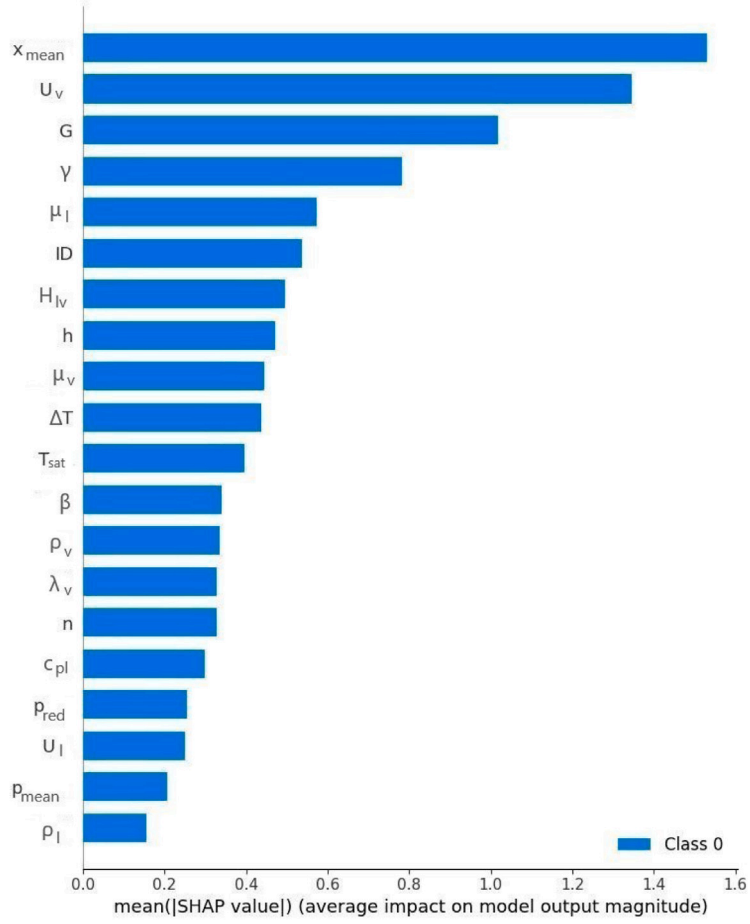

Fig. 7. SHAP values for prediction of HTC with dimensional data.

Table 8
Performance Metrics for FPD per unit of length prediction using non-dimensional data.

Method	MAE[a]	MSE[a]	RMSE[a]	R^2	MAE %
Linear Regression	0.030	0.0018	0.04	0.96	16.84%
XGBoost	0.018	0.001	0.034	0.97	10.14%
KNN	0.026	0.002	0.047	0.95	14.73%
Decision Tree	0.030	0.004	0.070	0.90	16.73%
Random Forest	0.017	0.001	0.035	0.97	9.45%
LightGBM	0.015	0.0008	0.029	0.98	8.45%
SVR	0.044	0.003	0.054	0.94	24.71%
Ridge Regression	0.030	0.0018	0.043	0.96	16.73%
Polynomial Regression	0.010	0.0002	0.014	0.99	5.98%
Elastic Net	0.190	0.055	0.23	0	104.67%
RANSAC Regressor	0.05	0.0061	0.078	0.89	27.73%
Artificial Neural Network	0.0080	0.0001	0.01	0.99	4.43%
Empirical model [41]	0.025	0.002	0.047	0.96	12.54%

[a] (bar/m)

ANN stands out as a standout performer, displaying good accuracy in both scenarios. In contrast to the HTC prediction scenario, transitioning from dimensional to non-dimensional data in FPD prediction results in a significant decrease in error metrics across many models. However, in the non-dimensional setting, some models, such as XGBoost, XGBlight, Random Forest, Decision Tree, and ANN, show an increase in errors. This anomaly suggests that these algorithms have a unique sensitivity to non-dimensional representations, emphasizing the importance of tailored considerations for specific models. Also, Polynomial Regression stands out for its remarkable consistency in producing reliable results, showcasing good performance among machine learning algorithms in FPD prediction tasks. In contrast to the HTC prediction scenario, it is noteworthy that, in the case of FPD prediction using non-dimensional data, the empirical model exhibits a relatively stronger performance. Despite the empirical model's comparatively better results, several ML and DL models (5 out of 12), such as XGBoost, Random Forest, LightGBM, Polynomial Regression, and ANN, still outperform it. This nuanced comparison underscores the effectiveness of advanced machine learning methodologies in FPD prediction, even when faced with a competitive empirical model.

5.1.3 Adaptability across data types

The analysis of both dimensional and non-dimensional datasets reveals consistent trends in algorithmic performance, with notable models such as XGBoost, Random Forest, LightGBM, and ANN demonstrating robust adaptability across the data's diverse nature. This adaptability is critical for addressing the complexities inherent in both dimensional and non-dimensional representations, highlighting the models' versatility. However, the subtle changes observed in specific models such as XGBoost, LightGBM, Random Forest, and Decision Tree during the transition from dimensional to non-dimensional data suggest that the optimal data type may vary depending on the model. This highlights the importance of a contextual analysis when determining the most suitable data representation for a particular predictive task. The results emphasize that, while certain models exhibit enhanced performance in the non-dimensional setting, the best-performing models, including XGBoost, Random Forest, LightGBM, and ANN, consistently

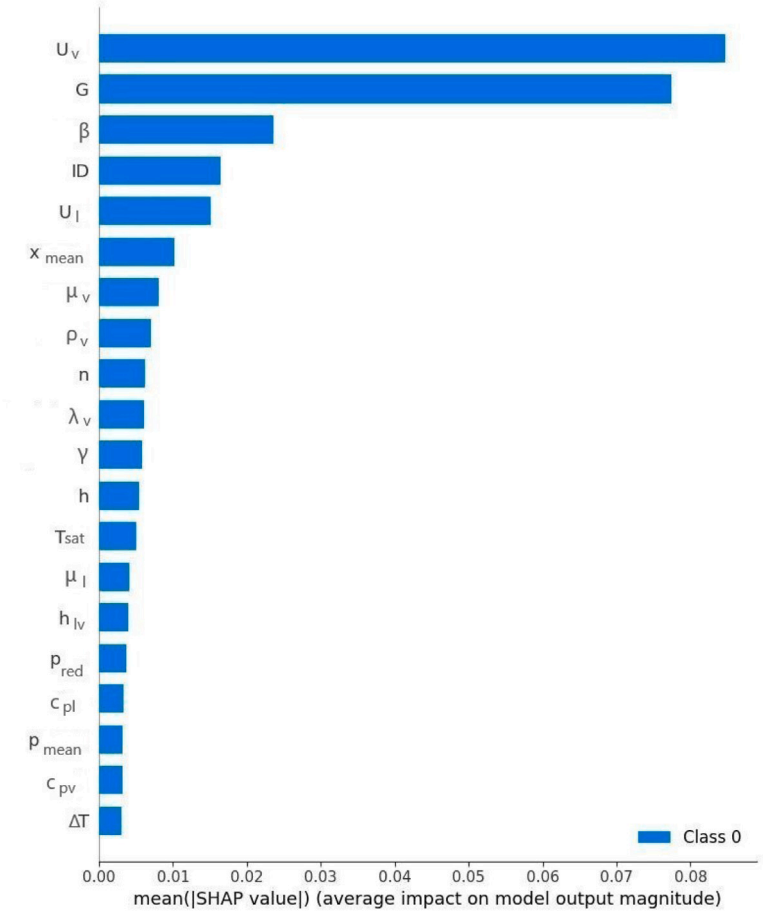

Fig. 8. SHAP values for prediction of FPD per unit of length with dimensional data.

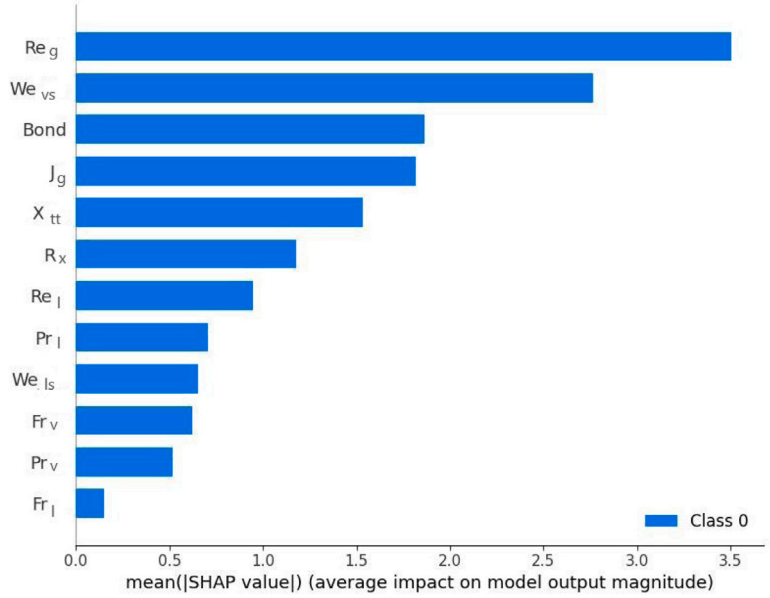

Fig. 9. SHAP values for prediction of HTC with non-dimensional data.

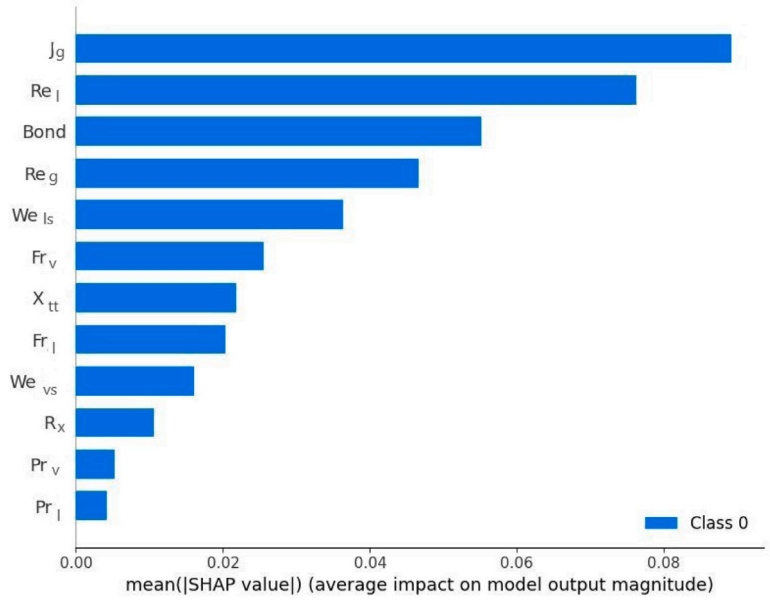

Fig. 10. SHAP values for prediction of FPD per unit of length with non-dimensional data.

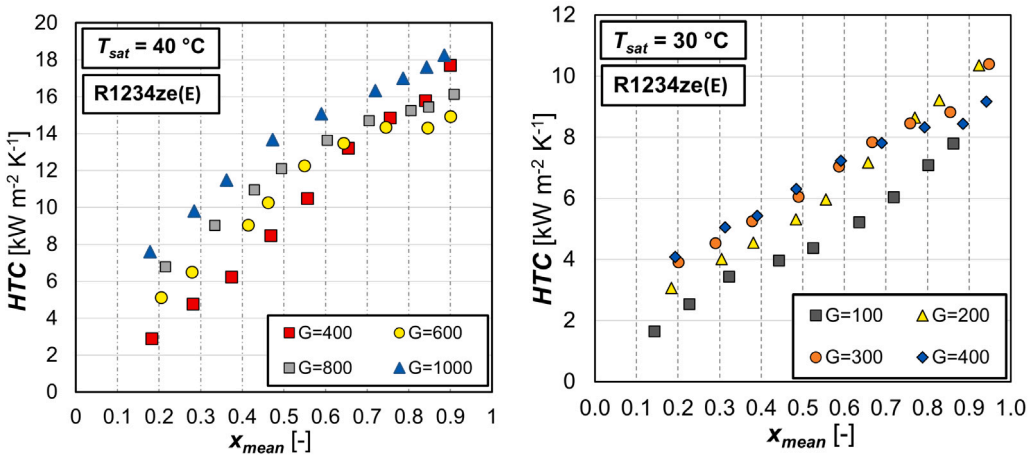

(a) 2.4mm ID (b) 6.14mm ID

Fig. 11. HTC versus vapor quality data from [9,24].

demonstrate superior accuracy with dimensional data. This insight emphasizes the importance of carefully selecting the data type that is aligned with the specific characteristics and requirements of the models used.

5.2 Thermal perspective

Regarding the implications of the results acquired by the comprehensive AI analyses, one could identify underlying thermal phenomena.

A. Regarding HTC, In Figs. 3 and 5 one could note that regardless of the type of input data, all models suffer from large deviations at high heat transfer coefficient (20–25 kW m^{-2} K^{-1}). Such occurrence is not unprecedented but on the contrary quite common in most empirical models developed for micro-finned tubes and often surmised to stem from an observed phenomenon that transpires at high values of mass flux inside micro-finned tubes. To elaborate, we must note the findings of [9,44–47] in which at high mass fluxes and vapor qualities, HTC reached an acme then slightly proceeded to decrease. The authors expressed that the unconventional occurrence is germane to the surface tension effect and the thickness of the condensate between the fins. In addition, in the assessment of the current database, it was discovered that the occurrence of such phenomena is highly dependent on tube diameter. For a pellucid illustration, one could refer to HTC versus vapor quality (x) in Fig. 11 for the 6.14 mm and 2.4 mm *ID*. As shown, another causality for the occurrence of such a peculiar trend can be related to the heat transfer area as well. Ultimately, we could link the high MAEs in ML and DL models at high HTCs to an unconventional pattern that seems to be abstruse to the AI models. For such reason, it is encouraged to feed ML and DL models with copious numbers of data points at high mass flux and vapor qualities to ameliorate the learning process.

B. From the assessment of SHAP values, we could infer that ML and DL models successfully identified underlying thermo-physical patterns during flow condensation. Concerning dimensional data, the precedence of U_v , x, and G whose variation and interplay have the essential rule in the prevailing flow pattern and consequently the liquid thickness which ultimately decides the heat transfer and pressure drop characteristics. For dimensionless SHAP values, the interplay of parameters is intriguing as the results are completely congruous with expectations. In this case, noting the discrepancies between Figs. 9 and 10, the importance of the Reynolds number should be highlighted. As attested, the frictional pressure drop is mostly due to the viscosity of the liquid phase, giving rise to the importance of Re_L as well as We_L in pressure drop assessment compared to HTC analysis. The bond number's importance in the output of the model was similarly reported by ML assessment of [17]. Further on, J_g and X_{tt} whose expressions are found on flow pattern maps [48–51] are main contributors to the prevailing flow pattern by considering the forces of inertia and gravity.

Overall, the proposed ANN model not only excels at the prediction of HTC and FPD at their high values, it successfully sheds light on the intricate interplay of physical and thermophysical parameters.

6 Conclusion

The article provided a comprehensive evaluation of ML and DL models in HTC and FPD prognostication inside micro-finned tubes which are the main tools in the design of heat exchangers. The training of the models was concluded on 1192 flow condensation data points acquired from the same laboratory with identical experimental techniques and experimental uncertainties which would minimize the range of noise in the data. Considering both dimensional and non-dimensional data as inputs. The following recapitulated results were concluded:

A. The sustained effectiveness of XGBoost, Random Forest, LightGBM, and ANN underscores their versatility and reliability.

B. The empirical model comparison emphasizes the advancements achieved through sophisticated modeling techniques. The nuanced changes in model performance when transitioning between dimensional and non-dimensional data underscore the importance of tailoring modeling approaches to the specific characteristics of the dataset.

C. Dimensionless groups could provide better accuracy for certain ML and DL models. However, it must be noted that the learning process is quite multifaceted, and the usage of dimensionless data as inputs as present in literature for empirical models does not guarantee an improved outcome.

D. In comparison with an empirical model of [3,41] for HTC and FPD respectively, AI models and their superiority, reinforce the potential of the ML and DL techniques in advancing the accuracy of heat transfer predictions.

E. The ability to capture intricate patterns and non-linear relationships within the data is a distinctive advantage of AI models, making them valuable tools in the realm of heat transfer research and engineering.

F. Except for the ANN model, all algorithms suffer from an inaccurate prediction at high values of HTC owing to the peculiar trend of HTC at high mass fluxes and vapor qualities inside micro-finned tubes which was concluded to be a function of tube diameter and its physical properties.

G. Owing to SHAP values, it is evident that correct underlying thermo-physical connections for flow condensation were identified by the ANN model.

H. Considering the attained results regarding the accuracy of the AI models, the design of condensers possessing horizontal tubes can be further facilitated. In the presence of preliminary data available, it is suggested that ANN and ML models identified as most promising in the following work be implemented to construct new predictive models. Overall, the classical empirical modeling which is vastly implemented for the design of heat exchangers could be replaced by ML and DL methods and the current paper further expands the insight into such a possibility.

7 Future work implications

A. The combination of mean average error recorded for the proposed ANN model and identification of underlying physical phenomena by utilization of SHAP values could abridge improvement operations on currently existing empirical correlations. In this case, it is surmised that such a model could be built on dimensionless groups of empirical correlations and help with the detection of parameters whose impact is more than one of the others.

B. In the field of explainable AI(XAI), researchers are increasingly recognizing the value of using asymmetric Shapley values instead of traditional methods to improve interpretability in ML models. The work [52] provides valuable insights into this emerging field. This study investigates new techniques for approximating asymmetric Shapley values using functional decomposition methodologies. The novelty of asymmetric Shapley values has resulted in a scarcity of readily available libraries, particularly in comparison to their vanilla Shapley counterparts. As a result, for many applications, using existing libraries is insufficient, necessitating the creation of custom implementations. While the implications of asymmetric Shapley values go beyond XAI, they are especially important in fields like heat transfer, where complex, asymmetric interactions between factors may influence system performance. In our future work, we hope to close this gap by focusing on our custom implementation for calculating asymmetric Shapley values in the design of heat exchangers with micro-finned tubes.

CRediT authorship contribution statement

Emad Efatinasab: Writing – original draft, Visualization, Validation, Software, Methodology. **Nima Irannezhad:** Writing – original draft, Visualization, Investigation, Formal analysis. **Mirco Rampazzo:** Writing – review & editing, Supervision. **Andrea Diani:** Writing – review & editing, Supervision, Project administration, Data curation, Conceptualization.

Declaration of competing interest

The authors declare that they have no known competing financial interests or personal relationships that could have appeared to influence the work reported in this paper.

Data availability

Data will be made available on request.

Appendix A

The evaluated heat transfer coefficient and frictional pressure drop values are included in Table A.1 as a function of mass flux and vapor quality.

Appendix B

In this section, we present prediction plots generated by other models under different scenarios (see Figs. B.1–B.4).

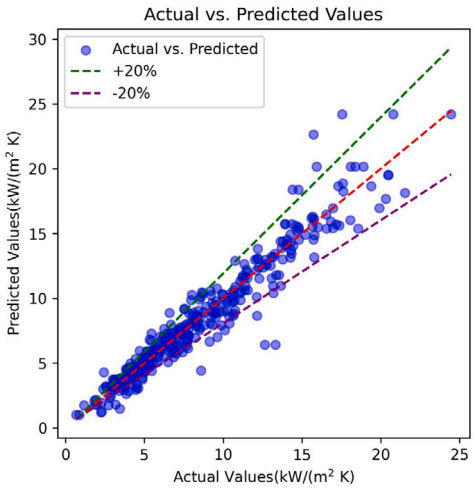

(a) HTC prediction of Decision Tree

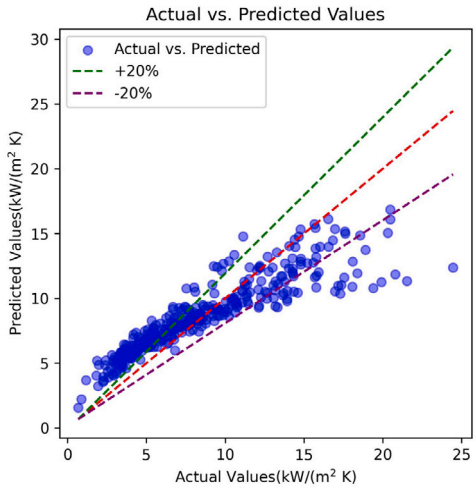

(b) HTC prediction of Elastic Net

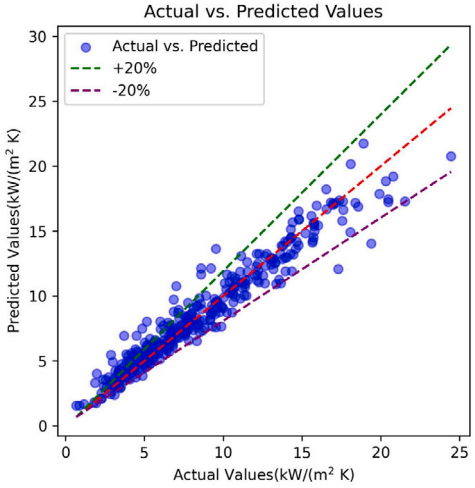

(c) HTC prediction of KNN

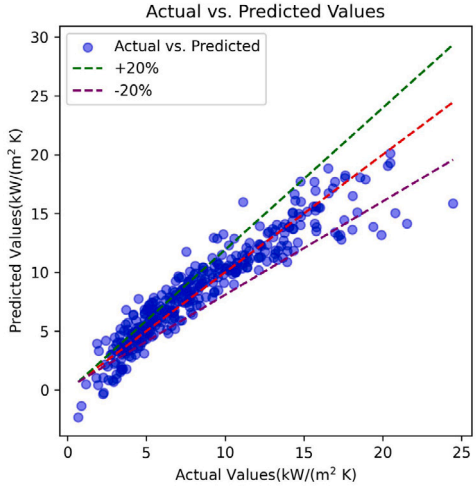

(d) HTC prediction of Linear Regression

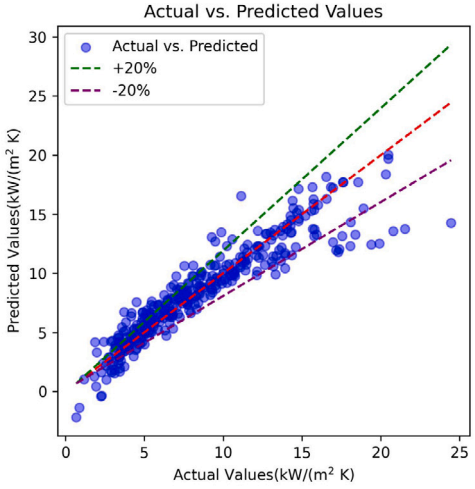

(e) HTC prediction of RANSAC Regressor

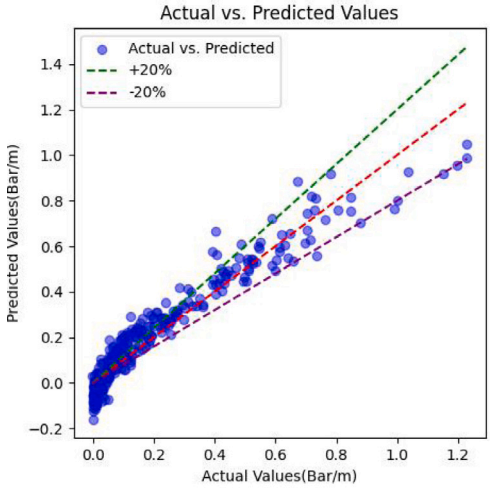

(f) HTC prediction of Ridge Regression

Fig. B.1. HTC prediction using dimensional data.

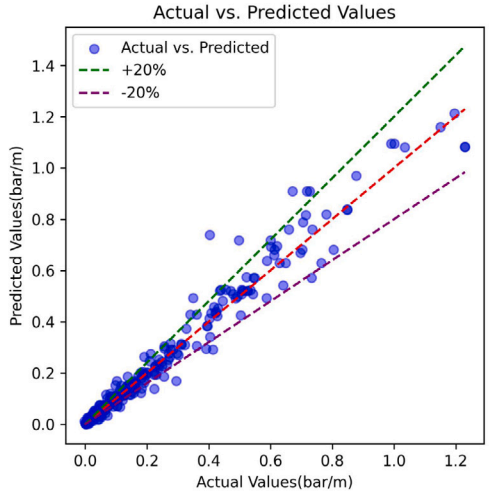

(a) FPD prediction of Decision Tree

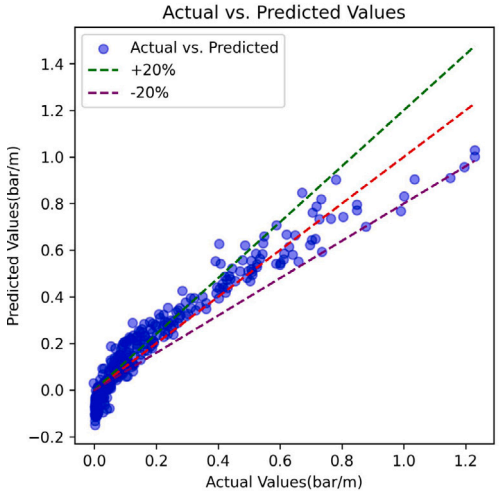

(b) FPD prediction of SVR

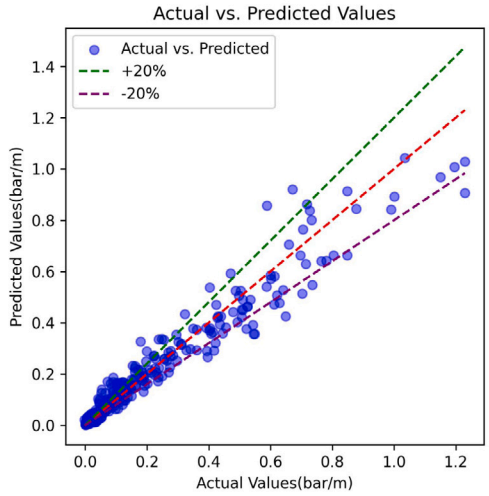

(c) FPD prediction of KNN

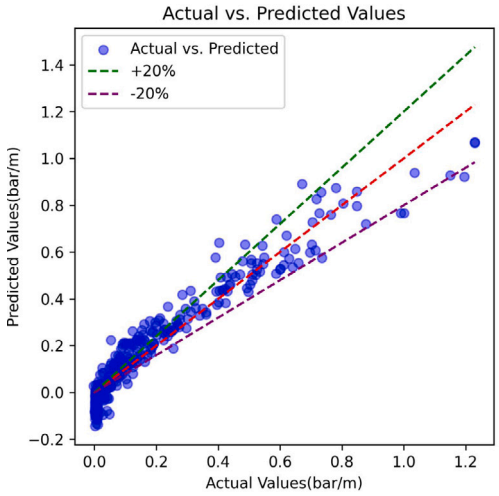

(d) FPD prediction of Linear Regression

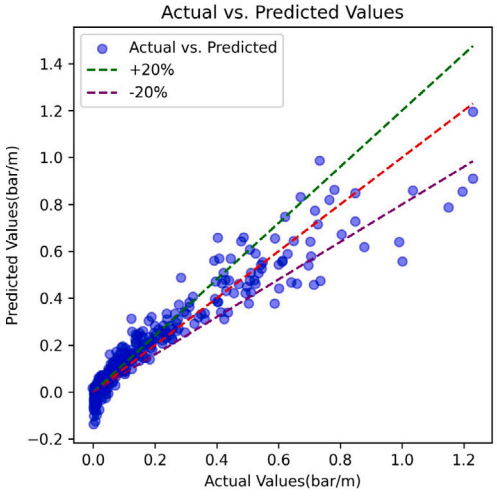

(e) FPD prediction of RANSAC Regressor

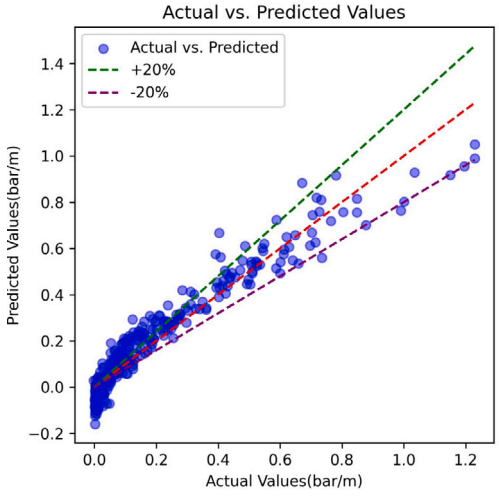

(f) FPD prediction of Ridge Regression

Fig. B.2. FPD prediction using dimensional data.

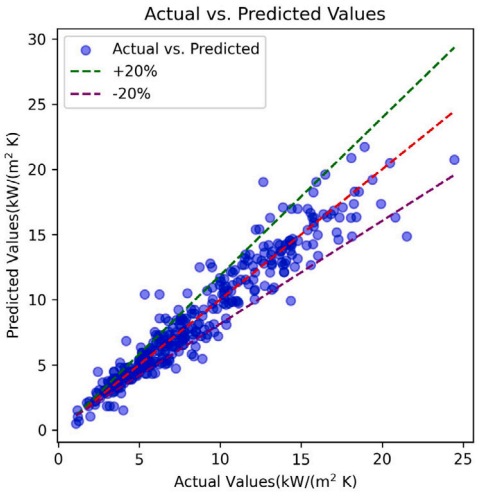

(a) HTC prediction of Decision Tree

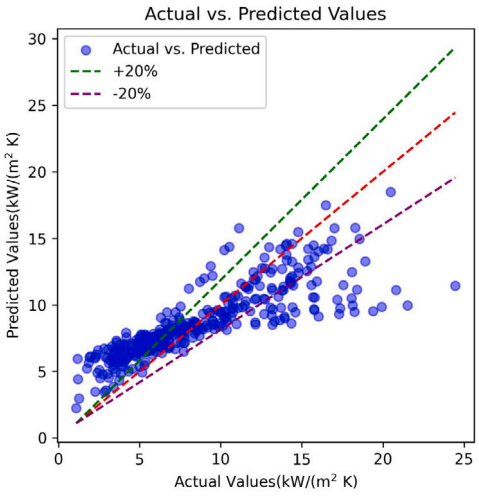

(b) HTC prediction of Elastic Net

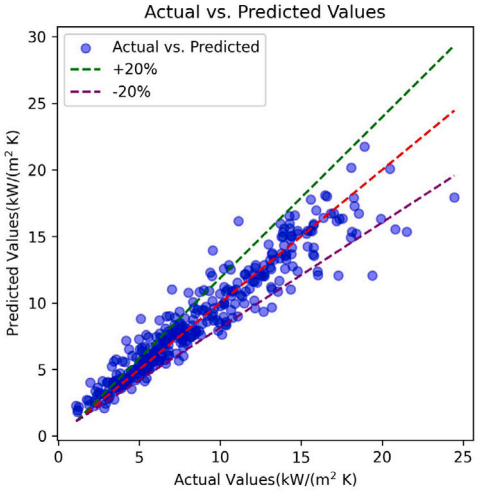

(c) HTC prediction of KNN

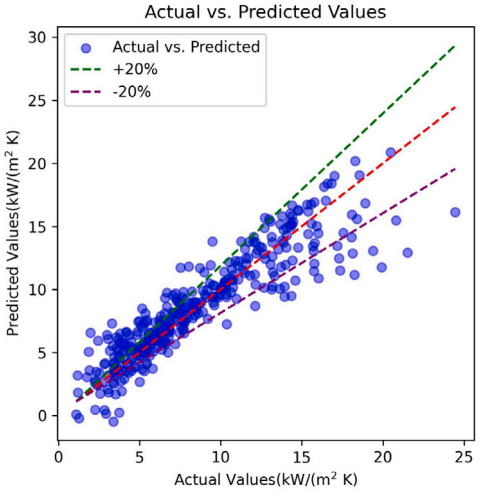

(d) HTC prediction of Linear Regression

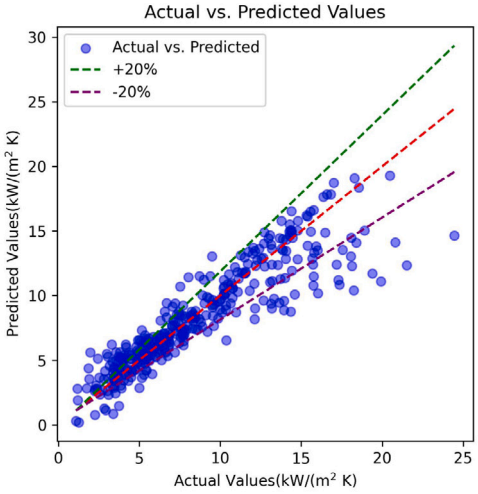

(e) HTC prediction of RANSAC Regressor

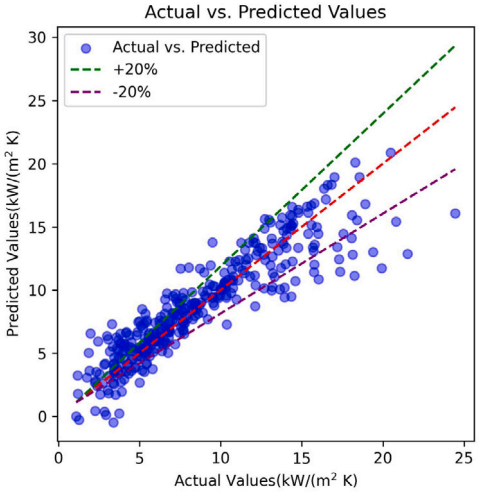

(f) HTC prediction of Ridge Regression

Fig. B.3. HTC prediction using non-dimensional data.

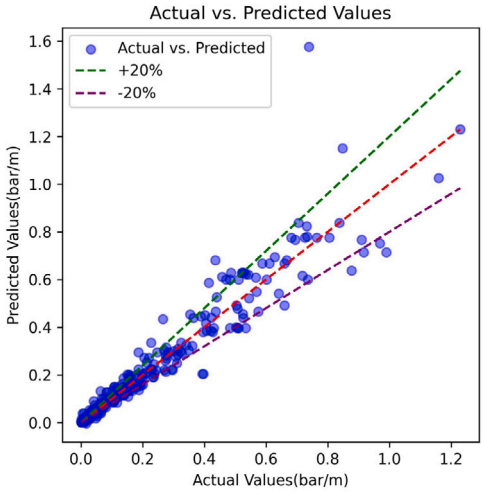

(a) FPD prediction of Decision Tree

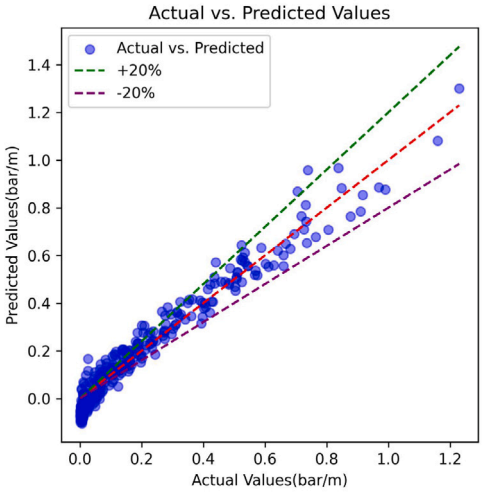

(b) FPD prediction of SVR

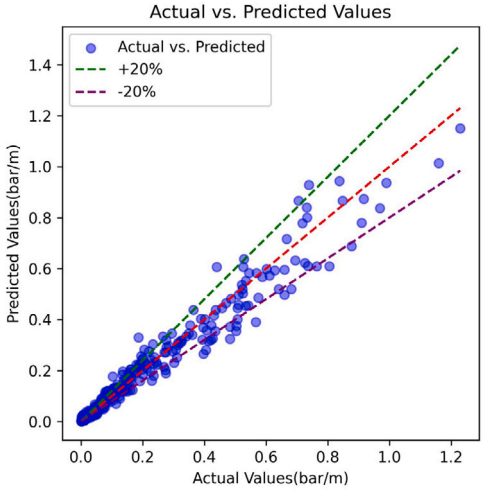

(c) FPD prediction of KNN

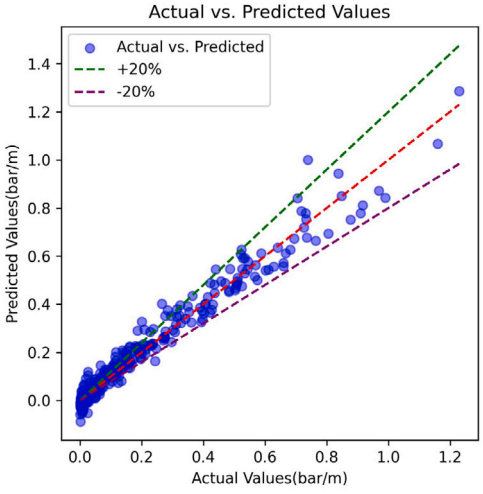

(d) FPD prediction of Linear Regression

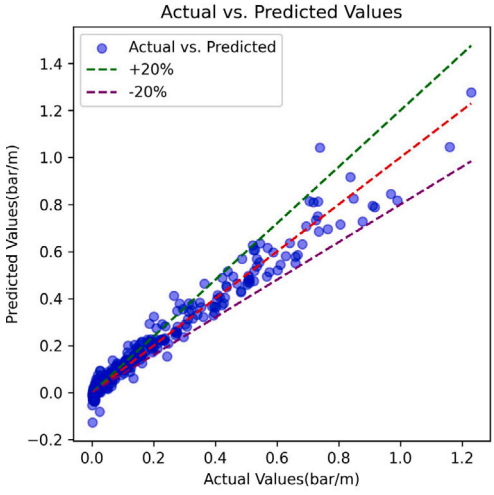

(e) FPD prediction of RANSAC Regressor

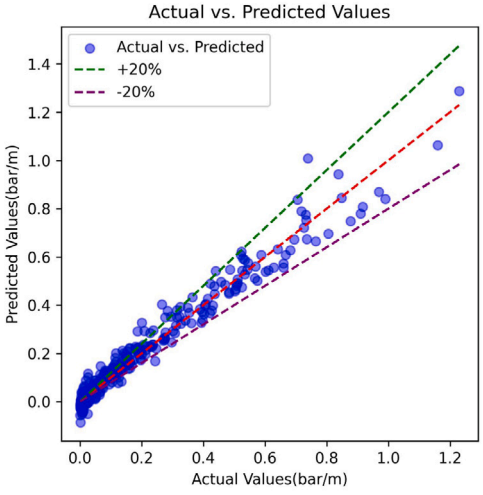

(f) FPD prediction of Ridge Regression

Fig. B.4. FPD prediction using non-dimensional data.

Table A.1
HTC and FPD per unit of length data as a function of mass flux and vapor quality.

Mass flux (kg m^{-2} s^{-1})	Vapor quality	HTC (W m^{-2} K^{-1})	FPD (Pa m^{-1})	T_{Sat} (° C)
605	0.13	5358	10 484	30
600	0.23	7145	15 950	30
602	0.35	8840	22 082	30
597	0.45	10 683	27 325	30
597	0.57	13 315	32 941	30
597	0.71	15 925	39 648	30
597	0.80	18 083	42 101	30
603	0.90	18 905	40 757	30
600	0.95	21 147	35 312	30
404	0.92	20 154	17 596	30
403	0.88	18 388	18 807	30
403	0.79	16 350	19 743	30
403	0.68	14 152	18 558	30
403	0.59	12 064	17 245	30
404	0.51	10 053	15 517	30
402	0.41	8432	13 230	30
402	0.31	6974	10 356	30
402	0.21	5668	7028	30
401	0.14	4730	5176	30
199	0.16	3867	1284	30
200	0.28	4863	1990	30
196	0.37	6032	2831	30
195	0.42	6709	3236	30
198	0.53	8227	4275	30
197	0.66	10 925	4922	30
196	0.75	13 436	5016	30
196	0.82	16 534	4809	30
197	0.91	18 667	4319	30
98	0.87	12 151	1004	30
97	0.80	10 108	989	30
97	0.72	8516	958	30
99	0.63	6582	846	30
98	0.54	5660	710	30
101	0.48	5158	549	30
101	0.34	5147	498	30
100	0.28	4340	397	30
101	0.18	2998	332	30
602	0.13	5153	8268	40
594	0.20	6011	11 136	40
596	0.29	7267	14 736	40
597	0.39	8363	18 692	40
599	0.48	9838	22 445	40
599	0.58	11 564	26 212	40
600	0.69	13 484	30 018	40
599	0.81	15 706	32 683	40
596	0.88	16 972	31 469	40
601	0.93	17 699	29 174	40
399	0.91	17 223	14 694	40
400	0.83	15 152	15 861	40
405	0.72	13 067	15 905	40
401	0.61	10 294	14 592	40
402	0.53	8468	13 014	40
402	0.42	7166	10 704	40
402	0.31	6261	8584	40
401	0.22	5183	6434	40
402	0.14	4325	4760	40
199	0.14	2818	1202	40
196	0.27	3810	1204	40
198	0.35	4567	1690	40
201	0.44	5428	2249	40
195	0.56	6716	2884	40
198	0.65	7807	3345	40
195	0.76	9974	3536	40
199	0.86	12 859	3621	40
198	0.90	14 973	3353	40
96	0.85	7548	629	40
100	0.80	7175	704	40
98	0.72	6026	606	40
100	0.65	5814	571	40
99	0.56	5454	494	40
101	0.48	5139	407	40
99	0.38	3815	456	40
99	0.29	2430	517	40
98	0.21	1825	125	40
96	0.19	1864	247	40
103	0.17	1499	204	40
151	0.22	3347	660	30
153	0.32	3938	888	30
150	0.40	4581	1100	30
146	0.48	5319	1280	30
150	0.62	7173	1186	30
151	0.70	8795	1416	30
146	0.77	9871	1356	30
148	0.83	11 725	1362	30
150	0.14	4009	650	30
152	0.21	4406	975	30
148	0.29	4908	1238	30
146	0.39	5797	1607	30
149	0.51	6840	1893	30
145	0.60	8028	2105	30
145	0.69	9506	2326	30
152	0.79	13 313	2762	30
151	0.86	16 749	2673	30
75	0.16	1364	219	30
76	0.20	1975	241	30
77	0.29	3311	291	30
77	0.44	5351	316	30
77	0.52	6062	367	30
76	0.64	6742	441	30
76	0.71	7228	479	30
76	0.76	7581	525	30
76	0.85	8668	549	30

References

[1] Cavallini A, Del Col D, Doretti L, Matkovic M, Rossetto L, Zilio C, et al. Condensation in horizontal smooth tubes: A new heat transfer model for heat exchanger design. Heat Transf Eng 2006;27:31–8. http://dx.doi.org/10.1080/01457630600793970.

[2] Kim S-M, Mudawar I. Universal approach to predicting heat transfer coefficient for condensing mini/micro-channel flow. Int J Heat Mass Transfer 2013;56:238–50. http://dx.doi.org/10.1016/j.ijheatmasstransfer.2012.09.032.

[3] Cavallini A, Del Col D, Mancin S, Rossetto L. Condensation of pure and near-azeotropic refrigerants in microfin tubes: A new computational procedure. Int J Refrig 2009;32:162–74. http://dx.doi.org/10.1016/j.ijrefrig.2008.08.004.

[4] Shah MM. An improved and extended general correlation for heat transfer during condensation in plain tubes. HVAC R Res 2009;15:889–913. http://dx.doi.org/10.1080/10789669.2009.10390871.

[5] Hirose M, Ichinose J, Inoue N. Development of the general correlation for condensation heat transfer and pressure drop inside horizontal 4 mm small-diameter smooth and microfin tubes. Int J Refrig 2018;90:238–48. http://dx.doi.org/10.1016/j.ijrefrig.2018.04.014.

[6] Zhang H, Fang X, Shang H, Chen W. Flow condensation heat transfer correlations in horizontal channels. Int J Refrig 2015;59:102–14. http://dx.doi.org/10.1016/j.ijrefrig.2015.07.013.

[7] Kim S-M, Mudawar I. Review of databases and predictive methods for pressure drop in adiabatic, condensing and boiling mini/micro-channel flows. Int J Heat Mass Transfer 2014;77:74–97. http://dx.doi.org/10.1016/j.ijheatmasstransfer.2014.04.035.

[8] Diani A, Cavallini A, Rossetto L. R1234yf condensation inside a 3.4 mm ID horizontal microfin tube. Int J Refrig 2017;75:178–89. http://dx.doi.org/10.1016/j.ijrefrig.2016.12.014.

[9] Diani A, Liu Y, Wen J, Rossetto L. Experimental investigation on the flow condensation of R450A, R515B, and R1234ze(E) in a 7.0 mm OD micro-fin tube. Int J Heat Mass Transfer 2022;196:123260. http://dx.doi.org/10.1016/j.ijheatmasstransfer.2022.123260.

[10] Li G-Q, Wu Z, Li W, Wang Z-K, Wang X, Li H-X, et al. Experimental investigation of condensation in micro-fin tubes of different geometries. Exp Therm Fluid Sci 2012;37:19–28. http://dx.doi.org/10.1016/j.expthermflusci.2011.09.008.

[11] Krzywanski J. A general approach in optimization of heat exchangers by bio-inspired artificial intelligence methods. Energies 2019;12(23). http://dx.doi.org/10.3390/en12234441, URL https://www.mdpi.com/1996-1073/12/23/4441.

[12] Nie F, Wang H, Zhao Y, Song Q, Yan S, Gong M. A universal correlation for flow condensation heat transfer in horizontal tubes based on machine learning.

Int J Therm Sci 2023;184:107994. http://dx.doi.org/10.1016/j.ijthermalsci.2022.107994.
[13] Azizi S, Ahmadloo E. Prediction of heat transfer coefficient during condensation of R134A in inclined tubes using artificial neural network. Appl Therm Eng 2016;106:203–10. http://dx.doi.org/10.1016/j.applthermaleng.2016.05.189.
[14] Balcilar M, Dalkilic A, Wongwises S. Artificial neural network techniques for the determination of condensation heat transfer characteristics during downward annular flow of R134A inside a vertical smooth tube. Int Commun Heat Mass Transfer 2011;38:75–84. http://dx.doi.org/10.1016/j.icheatmasstransfer.2010.10.009.
[15] Mattiuzzo N, Azzolin M, Berto A, Bortolin S, Del Col D. Condensation heat transfer and pressure drop of R1234yf/HFC mixtures inside small diameter channels. Int J Therm Sci 2023;189:108258. http://dx.doi.org/10.1016/j.ijthermalsci.2023.108258.
[16] Tarabkhah S, Sajadi B, Behabadi MAA. Prediction of heat transfer coefficient and pressure drop of R1234yf and R134a flow condensation in horizontal and inclined tubes using machine learning techniques. Int J Refrig 2023;152:256–68. http://dx.doi.org/10.1016/j.ijrefrig.2023.04.031.
[17] Hughes MT, Chen SM, Garimella S. Machine-learning-based heat transfer and pressure drop model for internal flow condensation of binary mixtures. Int J Heat Mass Transfer 2022;194:123109. http://dx.doi.org/10.1016/j.ijheatmasstransfer.2022.123109.
[18] Zhou L, Garg D, Qiu Y, Kim S-M, Mudawar I, Kharangate CR. Machine learning algorithms to predict flow condensation heat transfer coefficient in mini/micro-channel utilizing universal data. Int J Heat Mass Transfer 2020;162:120351. http://dx.doi.org/10.1016/j.ijheatmasstransfer.2020.120351.
[19] Lin L, Gao L, Kedzierski MA, Hwang Y. A general model for flow boiling heat transfer in microfin tubes based on a new neural network architecture. Energy AI 2022;8:100151. http://dx.doi.org/10.1016/j.egyai.2022.100151.
[20] Irannezhad N, Rossetto L, Diani A. A comprehensive study with high-speed camera assisted visualizations of HFO-1234ze(E) condensation inside an enhanced tube. Int Commun Heat Mass Transfer 2024;150:107203. http://dx.doi.org/10.1016/j.icheatmasstransfer.2023.107203.
[21] Diani A, Brunello P, Rossetto L. R513A condensation heat transfer inside tubes: Microfin tube vs. smooth tube. Int J Heat Mass Transfer 2020;152:119472. http://dx.doi.org/10.1016/j.ijheatmasstransfer.2020.119472.
[22] Diani A, Campanale M, Rossetto L. Experimental study on heat transfer condensation of R1234ze(E) and R134A inside a 4.0 mm OD horizontal microfin tube. Int J Heat Mass Transfer 2018;126:1316–25. http://dx.doi.org/10.1016/j.ijheatmasstransfer.2018.06.047.
[23] Diani A, Rossetto L. Condensation of an azeotropic mixture inside 2.5 mm ID minitubes. Fluids 2020;5:171. http://dx.doi.org/10.3390/fluids5040171.
[24] Diani A, Campanale M, Cavallini A, Rossetto L. Low GWP refrigerants condensation inside a 2.4 mm ID microfin tube. Int J Refrig 2018;86:312–21. http://dx.doi.org/10.1016/j.ijrefrig.2017.11.011.
[25] Kirkpatrick S, Gelatt CD, Vecchi MP. Optimization by simulated annealing. Science 1983;220(4598):671–80. http://dx.doi.org/10.1126/science.220.4598.671.
[26] Holland JH. Adaptation in Natural and Artificial Systems: An Introductory Analysis with Applications to Biology, Control and Artificial Intelligence. MIT Press; 1992.
[27] Kennedy J, Eberhart R. Particle swarm optimization. In: Proceedings of ICNN'95 - international conference on neural networks, vol. 4, 1995, p. 1942–8. http://dx.doi.org/10.1109/ICNN.1995.488968.
[28] Mirjalili S, Mirjalili SM, Lewis A. Grey wolf optimizer. Adv Eng Softw 2014;69:46–61. http://dx.doi.org/10.1016/j.advengsoft.2013.12.007.
[29] Noroozi M, Mohammadi H, Efatinasab E, Lashgari A, Eslami M, Khan B. Golden search optimization algorithm. IEEE Access 2022;10:37515–32. http://dx.doi.org/10.1109/ACCESS.2022.3162853.
[30] Hastie T, Tibshirani R, Friedman J. The elements of statistical learning. Springer series in statistics, New York, NY, USA; 2001.
[31] Chen T, Guestrin C. XGBoost: A scalable tree boosting system. New York, NY, USA: Association for Computing Machinery; 2016, p. 785–94. http://dx.doi.org/10.1145/2939672.2939785.
[32] Sauer J, Mariani VC, dos Santos Coelho L, Ribeiro MHDM, Rampazzo M. Extreme gradient boosting model based on improved Jaya optimizer applied to forecasting energy consumption in residential buildings. Evol Syst 2021;1–12.
[33] Cover T, Hart P. Nearest neighbor pattern classification. IEEE Trans Inform Theory 1967;13(1):21–7. http://dx.doi.org/10.1109/TIT.1967.1053964.
[34] Von Winterfeldt D, Edwards W. Decision analysis and behavioral research. 1986, (No Title).
[35] Breiman L. Random forests. Mach Learn 2001;45:5–32.
[36] Ke G, Meng Q, Finley T, Wang T, Chen W, Ma W, et al. LightGBM: A highly efficient gradient boosting decision tree. In: Advances in neural information processing systems, vol. 30, Curran Associates, Inc.; 2017.
[37] Hoerl AE, Kennard RW. Ridge regression: Biased estimation for nonorthogonal problems. Technometrics 1970;12(1):55–67. http://dx.doi.org/10.1080/00401706.1970.10488634.
[38] Zou H, Hastie T. Regularization and variable selection via the elastic net. J R Stat Soc Ser B Stat Methodol 2005;67(2):301–20.
[39] Stigler SM. Gergonne's 1815 paper on the design and analysis of polynomial regression experiments. Historia Math 1974;1(4):431–9. http://dx.doi.org/10.1016/0315-0860(74)90033-0.
[40] Fischler MA, Bolles RC. Random sample consensus: A paradigm for model fitting with applications to image analysis and automated cartography. Commun ACM 1981;24(6):381–95. http://dx.doi.org/10.1145/358669.358692.
[41] Diani A, Mancin S, Rossetto L. R1234ze (E) flow boiling inside a 3.4 mm ID microfin tube. Int J Refrig 2014;47:105–19.
[42] Lundberg SM, Lee S-I. A unified approach to interpreting model predictions. In: Guyon I, Luxburg UV, Bengio S, Wallach H, Fergus R, Vishwanathan S, Garnett R, editors. In: Advances in neural information processing systems, vol. 30, Curran Associates, Inc.; 2017, p. 4765–74.
[43] Frye C, Rowat C, Feige I. Asymmetric Shapley values: Incorporating causal knowledge into model-agnostic explainability. In: Proceedings of the 34th international conference on neural information processing systems. Red Hook, NY, USA: Curran Associates Inc.; 2020.
[44] Wu Z, Wu Y, Sundén B, Li W. Convective vaporization in micro-fin tubes of different geometries. Exp Therm Fluid Sci 2013;44:398–408.
[45] Longo GA, Mancin S, Righetti G, Zilio C. Comparative analysis of microfin vs smooth tubes in R32 and R410A condensation. Int J Refrig 2021;128:218–31.
[46] Graham D, Chato J, Newell T. Heat transfer and pressure drop during condensation of refrigerant R134A in an axially grooved tube. Int J Heat Mass Transfer 1999;42(11):1935–44.
[47] Irannezhad N, Rossetto L, Diani A. Flow condensation of low-GWP zeotropic mixtures inside 5 mm OD micro-finned tube. Appl Sci 2024;14(1). http://dx.doi.org/10.3390/app14010373.
[48] Zhuang X, Gong M, Chen G, Zou X, Shen J. Two-phase flow pattern map for R170 in a horizontal smooth tube. Int J Heat Mass Transfer 2016;102:1141–9. http://dx.doi.org/10.1016/j.ijheatmasstransfer.2016.06.094.
[49] Barbieri P, Jabardo J, Bandarra Filho E, et al. Flow patterns in convective boiling of refrigerant R-134A in smooth tubes of several diameters. In: Proceedings of the 5th European thermal-sciences conference, Eindhoven, The Netherlands. Citeseer; 2008, p. 18–22.
[50] Cavallini A, Censi G, Del Col D, Doretti L, Longo GA, Rossetto L. Condensation of halogenated refrigerants inside smooth tubes. HVAC&R Res 2002;8(4):429–51.
[51] El Hajal J, Thome J, Cavallini A. Condensation in horizontal tubes, part 1: two-phase flow pattern map. Int J Heat Mass Transfer 2003;46(18):3349–63. http://dx.doi.org/10.1016/S0017-9310(03)00139-X.
[52] Gevaert A, Saranti A, Holzinger A, Saeys Y. Efficient approximation of asymmetric Shapley values using functional decomposition. In: Holzinger A, Kieseberg P, Cabitza F, Campagner A, Tjoa AM, Weippl E, editors. Machine learning and knowledge extraction. Cham: Springer Nature Switzerland; 2023, p. 13–30.